RESEARCH PAPER

Fiber bundle topology optimization of hierarchical microtextures for wetting behavior in Cassie-Baxter mode

Yongbo Deng[1,2] · Weihong Zhang[3] · Zhenyu Liu[2] · Jihong Zhu[3] · Jan G. Korvink[1]

Abstract

This paper presents the topology optimization of hierarchical microtextures for wetting behavior in the Cassie-Baxter mode, considering a structural unit of the hierarchical microtexture composed of base and secondary structures. The geometrical configuration of the considered structural unit can be described as a fiber bundle composed of an external surface of the base structure and the pattern of the secondary structures. Thus, two design variables are defined, one for the external surface of the base structure, and the other for the pattern of the secondary structures. The Young-Laplace equation, including a term depending on the mean curvature of the external surface, is used to describe the liquid/vapor interface imposed with a surface tension in the Cassie-Baxter mode. To overcome the difficulty of numerically computing the second-order derivative of the external surface, two partial differential equation filters are sequentially applied to the design variable of the base structure to ensure the numerical accuracy and feasibility of using an efficient linear-element-based finite element method to solve the Young-Laplace equation. To improve the performance of the hierarchical microtextures, the volume of the liquid bulges suspended at the liquid/vapor interface in the Cassie-Baxter mode, before the transition into the Wenzel mode, is minimized to optimize the match between the external surface of the base structure and the pattern of the secondary structures. In the topology optimization process, penalization of the material density of the surface tension is achieved by an artificial Marangoni phenomenon. In numerical examples, solid surfaces are tiled into textures with axial symmetry, radial symmetry, chirality, and quasiperiodicity; and structural units are derived consisting of base structures with peak shapes and dense secondary structures surrounding the crests of the peaks. The optimized performance of the derived structural units has been confirmed by comparisons.

Keywords Topology optimization · Hierarchical microtextures · Material distribution method · Fiber bundle · Cassie-Baxter mode

Responsible Editor: Ole Sigmund

✉ Yongbo Deng
   yongbo.deng@kit.edu; yongbo_deng@hotmail.com

✉ Weihong Zhang
   zhangwh@nwpu.edu.cn

✉ Zhenyu Liu
   liuzy@ciomp.ac.cn

✉ Jihong Zhu
   jh.zhu@nwpu.edu.cn

✉ Jan G. Korvink
   jan.korvink@kit.edu

Extended author information available on the last page of the article.

1 Introduction

Microtextures have numerous applications in the control of wetting behaviors, because the texture morphology and surface free energy together determine the wettability of a substrate surface (Feng and Jiang 2006). Microtextures on a substrate surface can effectively modify the surface free energy and thus dominate the wetting behavior. Both the Wenzel and Cassie-Baxter wetting modes can exist on a textured solid surface (Wenzel 1936; Cassie and Baxter 1944). In the Wenzel mode, the liquid completely fills the microtextures. In the Cassie-Baxter mode, vapor pockets are trapped at the liquid/vapor interface supported by the microtextures. The wetting mode can transition from the Cassie-Baxter case to the Wenzel case when the liquid is pressurized by an increasing static pressure, enlarging the

volume of the liquid bulges suspended at the liquid/vapor interface and finally leading to the elimination of the vapor pockets. In this mode transition, the hydrophobicity of the solid surface is decreased because the surface free energy decreases with the filling of the microtextures by the liquid. A critical value of the static pressure exists at the mode transition of the wetting behaviors (Bico et al. 1999). Therefore, for a fixed static pressure imposed on the liquid, the performance of the microtextures and robustness of the Cassie-Baxter mode can be measured by the volume of the liquid bulges suspended at the liquid/vapor interface, where a smaller volume of the liquid bulges corresponds to a more robust Cassie-Baxter mode.

Several artificial microtextures have been reported to promote a robust Cassie-Baxter mode of wetting behavior on a solid surface (Wang et al. 2015). More efficient topology optimization has also been implemented for the design of microtextures with single-/overlayered geometries (Cavalli et al. 2013; Deng et al. 2018, 2019); these geometries can be fabricated by means of conventional photo-lithography processes, which are typical top-down processes at the microscale. Compared with the single-/overlayered case, hierarchical microtextures can support more metastable states of the Cassie-Baxter mode. Bottom-up processes, e.g., two-photon polymerization, have been developed for their fabrication (Kawata et al. 2001). This paper thus implements the topology optimization of hierarchical microtextures for wetting behavior in the Cassie-Baxter mode.

This topology optimization is an implementation by using the material distribution method, which was pioneered by Bendsøe and Kikuchi for elasticity (Bendsøe and Kikuchi 1988) and has been extended to several other scientific fields (Bendsøe and Sigmund 2003). Wettability control of solid surfaces using hierarchical microtextures is an aspect of fluid mechanics at material interfaces. With regard to fluid mechanics, topology optimization has been implemented by Borrvall and Petersson for Stokes flows (Borrvall and Petersson 2003), steady Navier-Stokes flows (Gersborg-Hansen et al. 2006), creeping fluid flows (Guest and Prévost

2006), unsteady Navier-Stokes flows (Kreissl et al. 2011; Deng et al. 2011), turbulent flows (Dilgen et al. 2018; Yoon 2016), and two-phase flows of immiscible fluids (Deng et al. 2017). With regard to hierarchical structures, several reports exist for elasticity and material design (Andreasen and Sigmund 2012; Wu et al. 2019; Xu et al. 2019; Rodrigues et al. 2002; Zhang and Sun 2006; Cadman et al. 2013; Huang et al. 2013; Yan et al. 2014; Guo et al. 2015; Xia and Breitkopf 2015; Sivapuram et al. 2016). With regard to material interfaces, related investigations have been implemented for stiffness and multi-material structures (Allaire et al. 2014; Vermaak et al. 2014; Sigmund and Torquato 1997; Gibiansky and Sigmund 2000; Gao and Zhang 2011; Luo et al. 2012; Yin and Ananthasuresh 2011; Wang and Wang 2004; Zhou and Wang 2007), layouts of shell structures (Krog and Olhoff 1996; Ansola et al. 2002; Hassani et al. 2013; Lochner-Aldinger and Schumacher 2014; Clausen et al. 2017; Dienemann et al. 2017), fluid-structure and fluid-particle interaction (Yoon 2010; Lundgaard et al. 2018; Andreasen 2020), energy absorption (Aulig and Lepenies 2012), cohesion (Behrou et al. 2017), and actuation (Raulli and Maute 2005).

The general design of hierarchical microtextures for wetting behavior in the Cassie-Baxter mode is sketched in Fig. 1a, where the structural unit is composed of base and secondary structures, as sketched in Fig. 1b. The sketched hierarchical microtexture can support metastable states of the Cassie-Baxter mode, which evolves as illustrated by cross-sectional views in Fig. 2a. When the liquid is pressurized by increasing the static pressure to which it is subjected, the Cassie-Baxter mode can evolve into a metastable state with increased curvature of the liquid/vapor interface. Once the static pressure has been sufficiently increased, the wetting behavior will transition into a state in which the liquid/vapor interface is completely supported by the secondary structures, as sketched in Fig. 2b. The Cassie-Baxter mode will begin to transition into the Wenzel mode if the liquid is pressurized further. In this paper, this state before the mode transition is referred to as the terminal state of the Cassie-Baxter mode
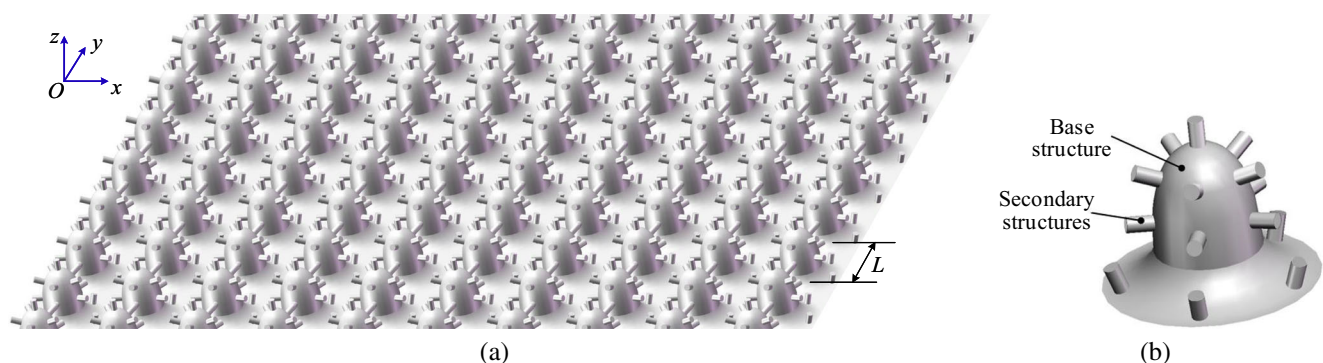

Fig. 1 (a) Sketch for the hierarchical microtextures with the structural unit composed of base and secondary structures, where L is the lattice size of the tiling on a solid surface. (b) Sketch for a structural unit composed of base and secondary structures
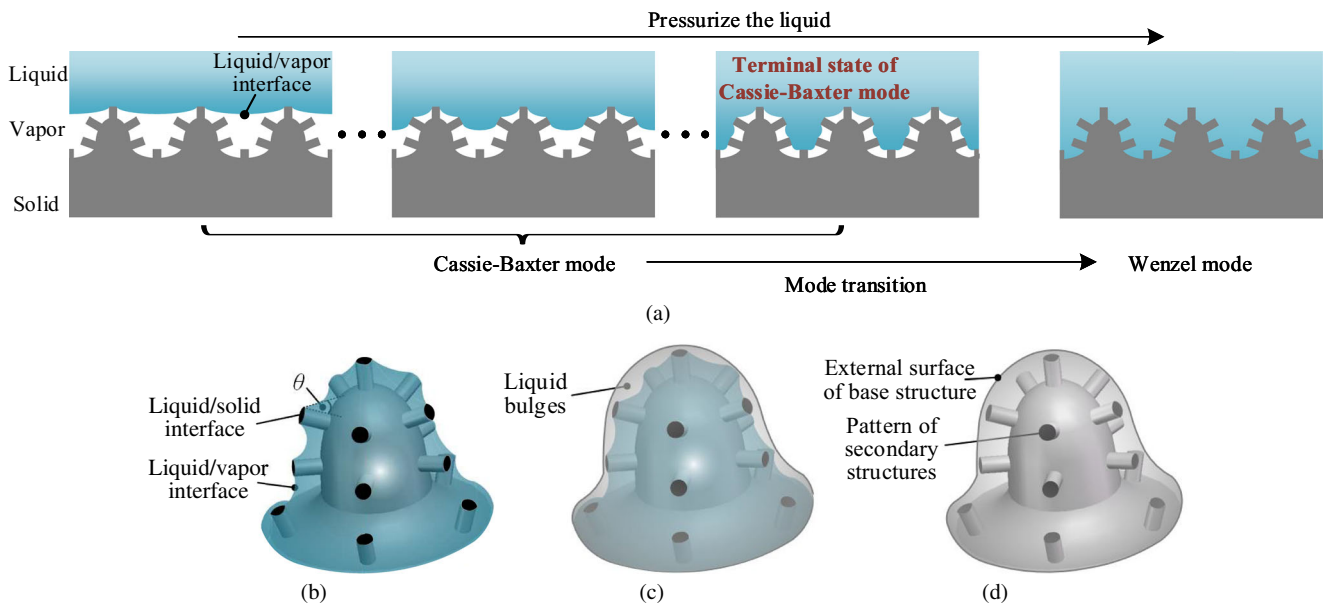
Fig. 2 (a) Cross-section demonstration for the evolution process of metastable states of the Cassie-Baxter mode, and the mode transition from a Cassie-Baxter case to a Wenzel case. (b) Sketch for the liquid/vapor interface completely supported by the secondary structures in the terminal state of the Cassie-Baxter mode, where θ is the contact angle at the sidewalls of the secondary structures. (c) Sketch for liquid bulges enclosed by the liquid/vapor interface and the external surface of the base structure. (d) Sketch for the external surface of the base structure and the pattern of the secondary structures

(Fig. 2a). The performance of hierarchical microtextures supporting wetting behaviors in the Cassie-Baxter mode can be measured by evaluating the volume of the liquid bulges suspended at the liquid/vapor interface in this terminal state. These liquid bulges are sketched in Fig. 2c, and the volume of interest is the one enclosed by the external surface of the base structure (Fig. 2d) and the liquid/vapor interface (Fig. 2b). Because a smaller volume of the liquid bulges corresponds to higher robustness of the Cassie-Baxter mode, topology optimization of the hierarchical microtextures is implemented in this paper by minimizing the volume of the liquid bulges in the terminal state of the Cassie-Baxter mode.

For the structural unit composed of base and secondary structures, the external surface (Fig. 2d) corresponding to the outer shape of the base structure can be described as a two-dimensional manifold (2-manifold). The pattern of the secondary structures (Fig. 2d) can then be defined on this 2-manifold. Here, the concept of a 2-manifold is used to exclude the possibility of a nonsmooth surface for the outer shape of the base structure, and to ensure that global differential operators can be well defined on this manifold (Chern et al. 1999). The external surface of the base structure and the pattern of the secondary structures together compose a fiber bundle (Chern et al. 1999). They represent the base manifold and the fibers of this fiber bundle, respectively. Once the description of the fiber bundle has been derived, the corresponding structural unit can be generated by applying an offset operation to the external surface of the base structure based on the

pattern of the secondary structures. The offset distance of this operation can be determined based on the criterion that the maximal value of the contact angle at the sidewalls of the secondary structures should be no larger than the critical advancing angle in the terminal state of the Cassie-Baxter mode. Therefore, the key point is to determine the fiber bundle that minimizes the volume of the liquid bulges in the terminal state of the Cassie-Baxter mode.

To determine the fiber bundle for hierarchical microtextures, topology optimization can be used to optimize the match between the external surface of the base structure and the pattern of the secondary structures. Thus, two design variables are defined, one for the external surface of the base structure and the other for the pattern of the secondary structures. To solve the optimization problems with two optimization variables corresponding to two sets of design parameters, combination among topology optimization, shape optimization, and optimal control has been implemented (Bendsøe 1995; Maute and Ramm 1997; Ansola et al. 2002; Hassani et al. 2013; Zhu et al. 2008; Christiansen et al. 2015a; Yang et al. 2018; Deng et al. 2014). The incipient combination of topology and shape optimization considered these two optimization techniques separately, by first seeking an optimal material layout and then refining the layout shape (Ansola et al. 2002). The subsequent combination for the optimization of structural patterns on curved surfaces was implemented by simultaneously optimizing the shape and material distribution of shell structures, where shape and topology iterations were

stacked alternately or carried out simultaneously (Ansola et al. 2002; Hassani et al. 2013). In those investigations, shape optimization was implemented by using CAD-based parametrization methods, where the curved surface was defined by means of control points to ensure a relatively small number of discretized design variables; during the optimization process, the finite element mesh was updated corresponding to the changes of the CAD model (Daoud et al. 2005). In topology optimization combined with optimal control (Deng et al. 2014), the control variable was normalized to have the same bound constraint as the design variable; the design and control variables were simultaneously evolved at the finite element nodes by using the method of moving asymptotes (Svanberg 1987).

In topology optimization of the hierarchical microtextures for wetting behavior in the Cassie-Baxter mode, the design variable of the secondary structures is defined on the external surface of the base structure. Thus, the design variable of the base structure implicitly describes the design domain of the secondary structures. The design variable of the base structure can be normalized to have the same bound constraint as that of the secondary structures. The two design variables can be simultaneously evolved at the finite element nodes by using the method of moving asymptotes.

During the optimization process, the design variable for the external surface of the base structure is filtered by two sequentially implemented partial differential equation (PDE) filters (Lazarov and Sigmund 2011), to derive the ordinate distribution on this surface defined on the xOy plane of a Cartesian system. These two PDE-filter operations are collectively referred to as a double PDE-filter approach. Compared with the filter techniques in the CAD-free parametrization used to ensure the smoothness of a surface (Jameson and Vassberg 2000; Daoud et al. 2005) and the double filter approach with a projection between the two filters used to allow for optimization of designs towards geometric variations (Christiansen et al. 2015b), the double PDE-filter approach in this paper has no projection and contributes to ensure the well-posedness of the topology optimization problem by regularizing the mean curvature of the external surface of the base structure, because a pressure term depending on this mean curvature is included in the Young-Laplace equation used to describe the liquid/vapor interface of the Cassie-Baxter mode. The design variable for the pattern of the secondary structures is then defined on the external surface of the base structure. During the optimization process, this design variable is sequentially filtered and projected by means of a surface-PDE filter and threshold projection to remove the blurriness and control the minimum length scale of the derived pattern, where the surface PDE filter defined on a curved surface is originated from the PDE filter defined on a flat plane (Wang et al. 2011; Guest et al. 2004).

The remaining sections of the paper are organized as follows. In Section 2, the methodology for topology optimization of hierarchical microtextures is introduced. In Section 3, results for different tilings of a solid surface are derived and discussed. The paper is concluded in Section 4. Acknowledgments are presented and an Appendix is provided at the end of this paper.

2 Methodology

Hierarchical microtextures on a solid surface usually exhibit some periodicity and symmetry (Toster and Lewis 2015). Such microtextures can be created by periodically paving the solid surface with repetitions of a certain structural unit corresponding to the tiling of the solid surface. Then, topology optimization of the hierarchical microtextures can be implemented for the structural unit instead of the whole hierarchical microtextures. Because of the scaling property of the solution to the Young-Laplace equation used to describe the liquid/vapor interface of the Cassie-Baxter mode, dimensionless modeling can be implemented in a three-dimensional (3D) Cartesian system with coordinates normalized with respect to the lattice size of the hierarchical microtextures. This approach simultaneously ensures the scaling generality of the derived results and enhances the accuracy of the numerical solution.

In the terminal state of the Cassie-Baxter mode, the liquid/vapor interfaces are fixed on the secondary structures of the hierarchical microtextures, where three-phase contact lines among the liquid, vapor, and solid are anchored at the corners corresponding to the pattern boundaries of the secondary structures. Then, an offset operation is required to be implemented to generate the corners corresponding to the pattern boundaries of the secondary structures. Because a structural unit of the hierarchical microtextures should preserve the dominant role of the surface tension and dimensionless modeling is implemented for the hierarchical microtextures, a scaling operation is required to be implemented on the dimensionless result to ensure the surface-to-volume ratio of the liquid/vapor interface to be much larger than 1, where the scaling factor is the lattice size and it can be found by compromising the performance and manufacturability of the hierarchical microtextures. Therefore, the structural unit can be obtained by applying offset and scaling operations to the fiber bundle corresponding to the optimized match between the external surface of the base structure and the pattern of the secondary structures (Fig. 3).

2.1 Modelling

In this section, description of the liuqid/vapor interface in the terminal state of the Cassie-Baxter mode, material
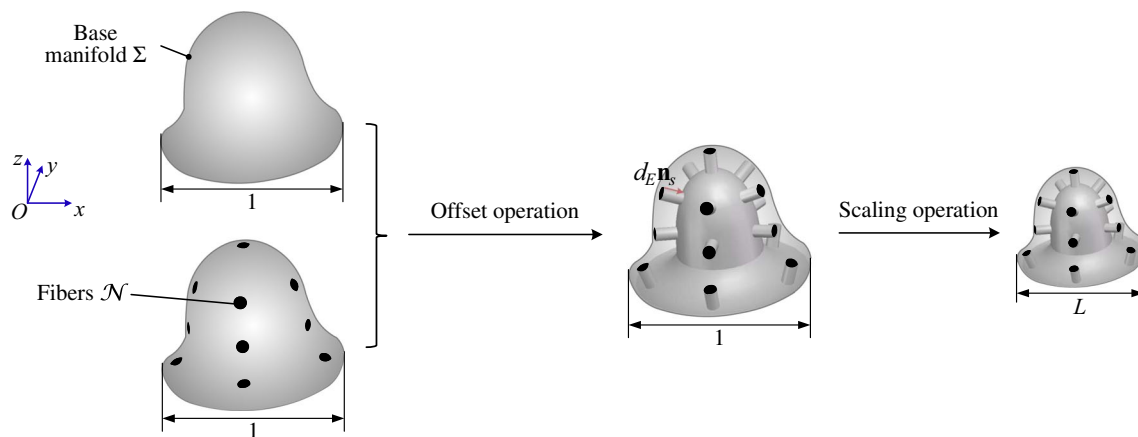
Fig. 3 Sketch for generating the structural unit based on offset and scaling operations of the fiber bundle, composed of the 2-manifold and the fibers, corresponding to the external surface of the base structure and the pattern of the secondary structures, respectively. Here, Σ is

the external surface of the base structure and $\mathcal{N}$ is the pattern of the secondary structures, $\mathbf{n}_s$ is the unitary normal direction of Σ, d_E is the offset distance of the offset operation, and the lattice size L is the scaling factor of the scaling operation

interpolation of the surface tension and performance measurement of the hierarchical microtextures are presented as follows.

2.1.1 Physical model and material interpolation

The interfaces among the solid, liquid, and vapor in the wetting behaviors can be assumed to be geometrical surfaces with zero thickness, when the characteristic size of these interfaces is much larger than the molecular scale. Based on the principle of free energy minimization at the interface of two immiscible fluids, the liquid/vapor interface supported by hierarchical microtextures is a surface with constant mean curvature determined by the static pressure imposed on the liquid. In the terminal state of the Cassie-Baxter mode, the liquid/vapor interface is completely supported by secondary structures, and the liquid/solid interface coincides with the pattern of the secondary structures. Based on Laplace's law, with a physical meaning of equilibrium between the capillary pressure and surface tension, the dimensionless Young-Laplace equation was derived to describe the liquid/vapor interface in the terminal state of the Cassie-Baxter mode (Young 1805; Laplace 1806):

$$2\bar{\sigma}_l H = 1, \text{ in } \Omega \setminus \Omega_{\mathcal{N}} \tag{1}$$

where $\bar{\sigma}_l = \sigma_l / (LP)$ is the dimensionless surface tension at the liquid/vapor interface, with σ_l, P, and L representing the surface tension, static pressure, and lattice size of the tiling on a solid surface, respectively; H is the mean curvature of the liquid/vapor interface in the 3D Cartisian system O-xyz; $\Omega \subset \mathbb{R}^2$, sketched in Fig. 4a, is an open, connected, and bounded two-dimensional (2D) domain localized in the xOy-plane and this domain is the dimensionless counterpart of the basic lattice used to tile a solid surface; $\Omega_{\mathcal{N}} \subset \Omega$ is the projection of $\mathcal{N}$ along z-axis in the xOy-plane, with $\mathcal{N}$ representing the pattern of the secondary structures.

As sketched in Fig. 4b, the convex liquid/vapor interface in the terminal state of the Cassie-Baxter mode is the graph of a multi-valued function defined on Ω, when the static pressure imposed on the liquid becomes large enough. Then the dimensionless Young-Laplace equation defined on Ω is singular and its numerical solution is difficult to converge, if the ordinate distribution on the liquid/vapor interface is used as the physical variable to describe the Cassie-Baxter mode and compute the mean curvature H. To solve this problem, the displacement of the liquid/vapor interface relative to the external surface of the base structure is used as the physical variable and the dimensionless Young-Laplace equation is thus transformed into the following formulation defined on a 2-manifold (Fig. 4c):

$$2\bar{\sigma}_l H_r = 1 - \kappa, \text{ on } \Sigma \setminus \mathcal{N} \tag{2}$$

where Σ is the 2-manifold corresponding to the external surface of the base structure, and it is the graph of a function defined on Ω; $\Sigma \setminus \mathcal{N}$ is the difference set between Σ and $\mathcal{N}$ as demonstrated in Fig. 4a; H_r is the mean curvature of the dimensionless liquid/vapor interface relative to the 2-manifold Σ; κ is referred to as the base pressure added to the constant static pressure in (1), and it is a variable static pressure dependent of the mean curvature of the external surface of the base structure. The base pressure is described as

$$\kappa = 2\bar{\sigma}_l H_\Sigma, \text{ in } \Omega \setminus \Omega_{\mathcal{N}} \tag{3}$$

where H_Σ is the mean curvature of Σ. The base pressure κ is finite, when the 2-manifold Σ is smooth and has no curvature singularity.

Because the liquid/solid interface coincides with the pattern of the secondary structures in the terminal state of the Cassie-Baxter mode, this interface has zero displacement relative to the external surface of the base structure. Therefore, the liquid/solid interface has zero mean curvature
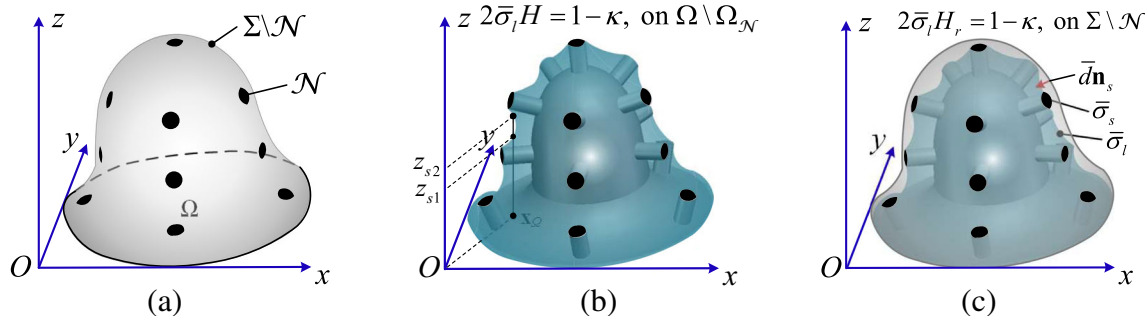
Fig. 4 (a) Sketch for the fiber bundle composed of the 2-manifold Σ and the fibers $\mathcal{N}$ corresponding to the external surface of the base structure and the pattern of the secondary structures, respectively. (b) Sketch for the description of the liquid/vapor interface by using the ordinate distribution on the liquid/vapor interface, where multi-valued points are caused by the convexity of the liquid/vapor interface and $\mathbf{x}_\Omega$ is a sketched multi-valued point in Ω corresponding to two different ordinates z_{s1} and z_{s2}. (c) Sketch for the description of the liquid/vapor interface by using the displacement of the liquid/vapor interface relative to the external surface of the base structure, where the multi-valued problem can be avoided

relative to the 2-manifold Σ. The dimensionless Young-Laplace equation defined on the 2-manifold Σ (2) has the equivalent form $H_r = (1 - \kappa) / (2\bar{\sigma}_l)$ on $\Sigma \setminus \mathcal{N}$. From this equivalent form, (2) can be extended onto $\mathcal{N}$ for the 2-manifold Σ with a smooth distribution of curvature. This extension can be implemented by setting an infinite dimensionless surface tension at the liquid/solid interface. Then, the zero relative mean curvature of the liquid/solid interface can be described as

$$H_r = \lim_{\bar{\sigma}_s \to +\infty} \frac{1 - \kappa}{2\bar{\sigma}_s} = 0, \text{ on } \mathcal{N} \tag{4}$$

where $\bar{\sigma}_s$ is the dimensionless surface tension at the liquid/solid interface. Based on this extension, the dimensionless Young-Laplace equation defined on the whole Σ can be described as

$$2\bar{\sigma} H_r = 1 - \kappa, \text{ on } \Sigma \tag{5}$$

where $\bar{\sigma}$ is the dimensionless surface tension at the two-phase interfaces consisted of the liquid/vapor and liquid/solid interfaces, satisfying $\bar{\sigma} = \bar{\sigma}_l$ at the liquid/vapor interface and $\bar{\sigma} = \bar{\sigma}_s \to +\infty$ at the liquid/solid interface. Simultaneously, the base pressure κ can be extended into the whole Ω as

$$\kappa = 2\bar{\sigma}_l H_\Sigma, \text{ in } \Omega \tag{6}$$

where the dimensionless surface tension is kept as $\bar{\sigma}_l$ to ensure the finite value of $(1 - \kappa)$, and the satisfaction of (4) on the liquid/solid interface.

On the 2-manifold Σ, a binary distribution can be defined to describe the pattern of the secondary structures as

$$\gamma_p = \begin{cases} 0, & \text{on } \mathcal{N} \\ 1, & \text{on } \Sigma \setminus \mathcal{N} \end{cases}, \tag{7}$$

where γ_p is the binary variable corresponding to the pattern of the secondary structures; the values of 0 and 1 correspond to the secondary structures and the void, respectively.

Based on this binary distribution, the dimensionless surface tension $\bar{\sigma}$ can be described as

$$\bar{\sigma}(\gamma_p) = \begin{cases} \bar{\sigma}_s, & \text{for } \gamma_p = 0 \\ \bar{\sigma}_l, & \text{for } \gamma_p = 1 \end{cases}. \tag{8}$$

The optimization task of this paper is to find the optimized match between the 2-manifold Σ and the binary distribution γ_p, corresponding to a minimal volume of the liquid bulges suspended at the liquid/vapor interface in the terminal state of the Cassie-Baxter mode. The binary optimization problem with $\gamma_p \in \{0, 1\}$ defined on a variable 2-manifold is difficult to solve numerically. Thus, the binary variable γ_p is relaxed to vary continuously in $[0, 1]$. The relaxed binary variable is referred to as the material density of the surface tension (Sigmund 2007).

The non-uniform distribution of the material density causes the gradient of the surface tension. In the topology optimization process, the material density is evolved by using the sensitivity of the design objective; correspondingly, the gradient of the surface tension is changed and this actuates the evolution of the liquid-vapor interface. When the optimization process converges, the evolution of the liquid-vapor interface is stopped, because the intermediate material density valued between 0 and 1 is removed and the gradient of the surface tension vanishes on the liquid/vapor and liquid/solid interfaces, respectively. This process, which achieves a penalization of the intermediate material density, can correspond to a Marangoni phenomenon (Vanhook et al. 1997). Based on this Marangoni phenomenon, the material interpolation of topology optimization is implemented by using the material density of the surface tension.

On the implementation of material interpolation, several schemes have been developed, and are summarized in the references of Bendsøe and Sigmund (1999) and Hvejsel and Lund (2011). In this paper, the convexity of the liquid/vapor interface is sensitive to the surface tension value. The convex and q-parameterized interpolation scheme is chosen

to implement the material interpolation of the dimensionless surface tension as (Borrvall and Petersson 2003)

$$\bar{\sigma}\left(\gamma_p\right) = \bar{\sigma}_l + \left(\bar{\sigma}_s - \bar{\sigma}_l\right) q \frac{1 - \gamma_p}{q + \gamma_p}, \tag{9}$$

where $\bar{\sigma}\left(\gamma_p\right)$ is the interpolated dimensionless surface tension; q is the parameter used to tune the convexity of the interpolation function. Theoretically, $\bar{\sigma}_s$ should be infinite; numerically, a finite but large enough value satisfying $\bar{\sigma}_s \gg \sup_{\Omega} |\kappa|$ can be chosen for $\bar{\sigma}_s$, to simultaneously ensure the stability of the numerical implementation and approximate the liquid/solid interface with an acceptable tolerance, where sup is the operator used to extract the suprema of a function.

During the optimization process, the external surface of the base structure is evolved iteratively, where the suprema of $|\kappa|$ cannot be determined in advance. This can result in losing an approximation of equation 6 and penalization of the intermediate material density, because the preset value of $\bar{\sigma}_s$ can violate $\bar{\sigma}_s \gg \sup_{\Omega} |\kappa|$ in some iterations. To solve this problem, material interpolation can be imposed on the base pressure in equation 5. This interpolation should be able to better determine the liquid/solid interface by eliminating the base pressure from the pattern of the secondary structures and maintaining its existence at the liquid/vapor interface. Therefore, the interpolation of the base pressure is implemented by multiplying it with

$$p_\kappa\left(\gamma_p\right) = p_{\kappa,\max} + \left(p_{\kappa,\min} - p_{\kappa,\max}\right) q \frac{1 - \gamma_p}{q + \gamma_p}, \tag{10}$$

where the convex and q-parameterized scheme is chosen; p_κ is the penalization factor; $p_{\kappa,\min} = 0$ and $p_{\kappa,\max} = 1$ are the minimal and maximal values of p_κ, respectively. Based on this interpolation, the base pressure can be eliminated at the liquid/solid interface by $p_\kappa\left(\gamma_p\right) = p_{\kappa,\min} = 0$, where γ_p is equal to 0; conversely, it is maintained without change at the liquid/vapor interface by $p_\kappa\left(\gamma_p\right) = p_{\kappa,\max} = 1$, where γ_p is equal to 1.

Based on the differential computation of the mean curvature, and the material interpolation of the dimensionless surface tension and the base pressure, the dimensionless Young-Laplace equation with the normalized displacement of the two-phase interfaces relative to the 2-manifold Σ can be derived as

$$\begin{cases} \begin{cases} \nabla_s \cdot \left[\bar{\sigma}\left(\gamma_p\right) \frac{\nabla_s \bar{d}}{\sqrt{1/d_0^2 + |\nabla_s \bar{d}|^2}}\right] = 1 - p_\kappa\left(\gamma_p\right) \kappa\left(z_s\right), \text{ on } \Sigma \\ \bar{d} = 0, \text{ at } \partial\Sigma \end{cases} \\ \kappa\left(z_s\right) = \bar{\sigma}_l \nabla \cdot \left(\frac{\nabla z_s}{\sqrt{1 + |\nabla z_s|^2}}\right), \text{ in } \Omega \\ \bar{\sigma}\left(\gamma_p\right) = \bar{\sigma}_l + \left(\bar{\sigma}_s - \bar{\sigma}_l\right) q \frac{1 - \gamma_p}{q + \gamma_p} \\ p_\kappa\left(\gamma_p\right) = p_{\kappa,\max} + \left(p_{\kappa,\min} - p_{\kappa,\max}\right) q \frac{1 - \gamma_p}{q + \gamma_p} \end{cases}, \tag{11}$$

where ∇_s is the surface gradient operator defined on Σ; $\bar{d}$ is the normalized displacement of the two-phase interfaces relative to the 2-manifold Σ (Fig. 4c); d_0 is the magnitude of the displacement of the two-phase interfaces; z_s is the ordinate distribution on the 2-manifold Σ; to consider more periodicity (e.g., chirality and quasiperiodicity) beyond axial symmetry, the periodicity of the solution of equation 11 is enforced by imposing a homogeneous boundary condition on $\bar{d}$, i.e., the two-phase interfaces are constrained by setting $\bar{d} = 0$ at $\partial\Sigma$ to ensure the solution uniqueness of equation 11 and fix the external surface of the base structure on the skeletons of the tiling of a solid surface, and this can permit to periodically pave the solid surface with a derived structural unit. In (11), the magnitude d_0 is used to normalize the dimensionless displacement of the two-phase interfaces. This can effectively enhance the accuracy of the numerical solution to (11), and the dimensionless displacement of the two-phase interfaces relative to the external surface of the base structure can be computed as $d_0 \bar{d}$.

2.1.2 Performance measurement

The performance of the microtextures used to control the wetting behavior in the Cassie-Baxter mode can be measured by the volume of the liquid bulges suspended at the liquid/vapor interface, because a smaller volume of the liquid bulges corresponds to more robust Cassie-Baxter mode (Deng 2018, 2019). A similar performance measurement can also be adopted to evaluate the terminal state of the Cassie-Baxter mode, for which the liquid bulges enclosed by the liquid/vapor interface and the external surface of the base structure have been sketched in Fig. 4c. To ensure the numerical stability of the optimization process, the performance of the hierarchical microtextures is equivalently measured by the following well-posed formulation:

$$J = \frac{1}{|\Sigma|^2} \int_{\Sigma} \bar{d}^2 \, d\Sigma, \tag{12}$$

where $|\Sigma|$ is the area of Σ, and it is computed as

$$|\Sigma| = \int_{\Sigma} 1 \, d\Sigma. \tag{13}$$

Because of the norm equivalence in the first-order Sobolev space $\mathcal{H}\left(\partial\Sigma\right)$ (Hebey 1996), the performance measurement in (12) is equivalent to the square of the normalized volume of the liquid bulges $\left(\int_{\Sigma} |\bar{d}| \, d\Sigma / |\Sigma|\right)^2$.

2.2 Design variables

To optimize the match between the external surface of the base structure and the pattern of the secondary structures by minimizing the volume of the liquid bulges suspended at the liquid/vapor interface in the terminal state of the

Cassie-Baxter mode, it is required to define two design variables for the external surface of the base structure and the pattern of the secondary structures, respectively.

2.2.1 Design variable of base structure

To describe the external surface of the base structure, a design variable z_m that takes continuous values in [0, 1] is defined for the ordinate distribution on the 2-manifold Σ, which is the design domain for the pattern of the secondary structures. To control the smoothness of this design variable, it is filtered by a PDE filter (Lazarov and Sigmund 2011):

$$\begin{cases} -\nabla \cdot \left(r_m^2 \nabla z_f \right) + z_f = z_m, & \text{in } \Omega \\ z_f = 0, & \text{on } \partial\Omega \end{cases}, \qquad (14)$$

where z_f is the filtered design variable; r_m is the filter radius, which is constant. Then, the filtered design variable z_f is further smoothed by implementing a similar PDE-filter operation to derive the ordinate distribution z_s of Σ and control the height of the structural unit:

$$\begin{cases} -\nabla \cdot \left(r_m^2 \nabla z_s \right) + z_s = b_z z_f, & \text{in } \Omega \\ z_s = 0, & \text{on } \partial\Omega \end{cases}, \qquad (15)$$

where $\nabla = \frac{\partial}{\partial x}\mathbf{i} + \frac{\partial}{\partial y}\mathbf{j}$ is the gradient operator on the xOy-plane; $\mathbf{i}$ and $\mathbf{j}$ are the unitary directional vectors of x and y axes, respectively; b_z is a specified height amplitude of the structural unit and it is nonnegative. It has been mentioned that the approach used to regularize the design variable of the base structure by using two sequentially implemented PDE filters is referred to as a double PDE-filter

approach, which is sketched in Fig. 5 including the related quantities.

The design variable of the base structure and the two PDE filters in the double PDE-filter approach can determine a differential homeomorphism corresponding to the bijection $\mathbf{x}_\Sigma = \mathbf{x}_\Omega + z_s(\mathbf{x}_\Omega)\mathbf{k}$ for $\forall \mathbf{x}_\Omega \in \Omega$, where $\mathbf{x}_\Omega$ and $\mathbf{x}_\Sigma$ are the points on Ω and Σ, respectively, $z_s(\mathbf{x}_\Omega)$ is the ordinate distribution of Σ, and $\mathbf{k}$ is the unitary directional vector of z axis of the 3D Cartesian system. Therefore, Σ is a 2-manifold immersed in $\mathbb{R}^2$.

From the PDE filter in (15) with a constant filter radius, $\nabla^2 z_s = \left(z_s - b_z z_f \right)/r_m^2$ can be obtained; further, the base pressure κ in (11) can be transformed into the following form based on the two PDE filters for the design variable of the base structure:

$$\begin{aligned} \kappa &= 2\bar{\sigma}_l H_\Sigma \\ &= \bar{\sigma}_l \nabla \cdot \left(\frac{\nabla z_s}{\sqrt{1 + |\nabla z_s|^2}} \right) \\ &= \bar{\sigma}_l \frac{\nabla^2 z_s}{\sqrt{1 + |\nabla z_s|^2}} - \bar{\sigma}_l \frac{(\nabla z_s \cdot \nabla z_s)\nabla^2 z_s}{\left(\sqrt{1 + |\nabla z_s|^2} \right)^3} \\ &= \frac{\bar{\sigma}_l}{r_m^2} \left[\frac{z_s - b_z z_f}{\sqrt{1 + |\nabla z_s|^2}} - \frac{|\nabla z_s|^2 \left(z_s - b_z z_f \right)}{\left(\sqrt{1 + |\nabla z_s|^2} \right)^3} \right] \\ &= \frac{\bar{\sigma}_l}{r_m^2} \frac{z_s - b_z z_f}{\left(\sqrt{1 + |\nabla z_s|^2} \right)^3}. \end{aligned} \qquad (16)$$
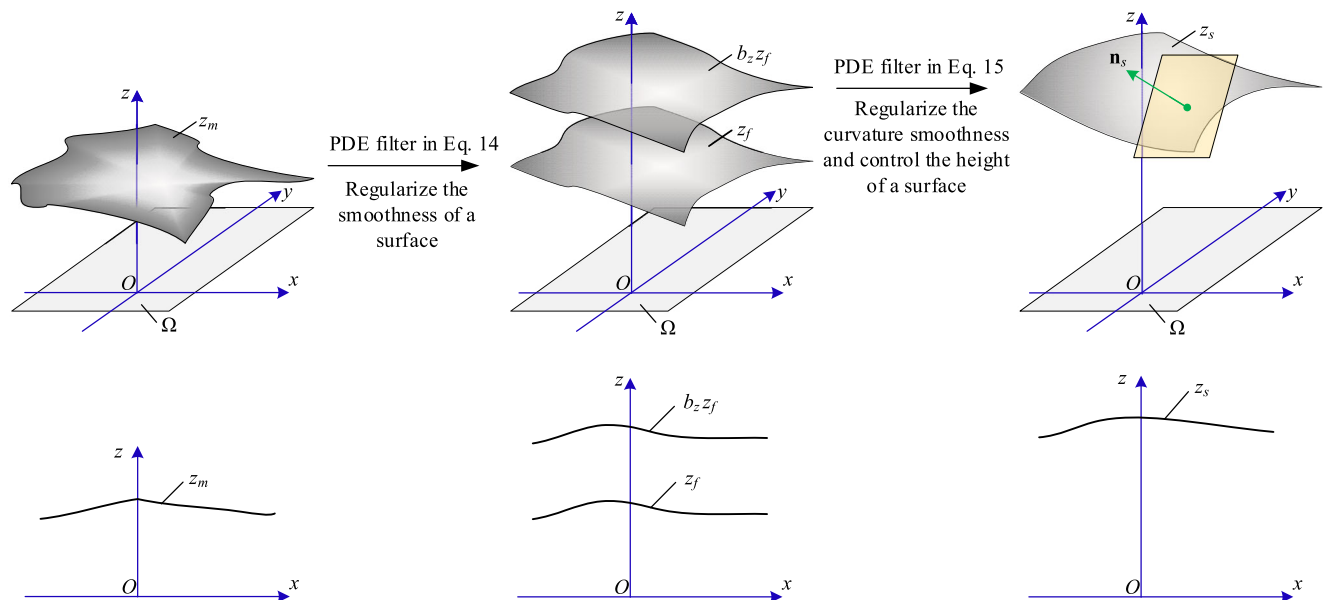

Fig. 5 Sketch for the double PDE-filter approach used to regularize the design variable of the base structure, where the second row contains the cross-sectional views of the sketch in the first row. In this sketch, z_m, z_f, and z_s are the design variable, filtered design variable, and ordinate distribution on the 2-manifold Σ, respectively; b_z is a specified height amplitude of the structural unit; Ω is the dimensionless lattice of a tiling; $\mathbf{n}_s$ is the unitary normal vector of Σ

The transformation of the base pressure shows that the double PDE-filter approach can eliminate the second-order derivative in the mean curvature of the external surface of the base structure. Because the second-order derivative in the base pressure can not be directly eliminated in the Galerkin variational of the dimensionless Young-Laplace (11), the transformation of the base pressure can effectively ensure the numerical accuracy and feasibility of using the efficient linear-element-based finite element method to solve the dimensionless Young-Laplace equation.

The transformed base pressure in (16) depends on z_s and z_f, both of which are functions in $\mathcal{H}(\Omega)$. The finite element solutions of z_s and z_f are functions in the infinite smooth function space $\mathcal{C}^\infty(\bar{\Omega})$, which is dense in $\mathcal{H}(\Omega)$; here, $\bar{\Omega}$ is the closure of Ω. The double PDE-filter approach can thus provide a well-posed approach to ensure the curvature smoothness of a surface. It has been specified that the precondition for using the liquid/vapor interface to approximate the liquid/solid interface is the curvature smoothness of the 2-manifold Σ. Therefore, the double PDE-filter approach can effectively ensure the well-posedness of the topology optimization problem, by avoiding the non-smoothness of the curvature caused by the design variable $z_m \in \mathcal{H}^{-1}(\Omega)$, where $\mathcal{H}^{-1}(\Omega)$ is the dual space of $\mathring{\mathcal{H}}(\Omega)$ representing the closure of the compactly supported and infinitely smooth function space $\mathcal{C}_0^\infty(\Omega)$.

The double PDE-filter approach increases the CPU-time cost of solving the topology optimization problem, although it can ensure the smoothness of a surface's curvature. If the second PDE filter is removed, this approach will degenerate into the single PDE-filter approach similar to Bletzinger's CAD-free approach (Daoud et al. 2005), which can ensure the surface smoothness instead of the curvature smoothness. Bletzinger's CAD-free approach has been implemented on curved surfaces, e.g., the cylindrical surface; the current double PDE-filter approach is implemented on the xOy-plane, and this approach can be extended to curved surfaces. In the extension, the PDE filters will be replaced by the surface-PDE filters (Deng et al. 2020). If a projection is added between the two filters, this double PDE-filter approach can turn into a similar one suggested in the reference of Christiansen et al. (2015b).

2.2.2 Design variable of secondary structures

To implement the material interpolation of the surface tension, a design variable γ takes continuous values in [0, 1] as defined on the 2-manifold Σ with the ordinate distribution z_s. The material density of the surface tension can be derived by smoothing and projecting the design variable γ, on which a surface-PDE filter (Lazarov and Sigmund 2011; Deng et al. 2020) and threshold projection (Wang et al. 2011; Guest et al. 2004) are implemented

sequentially. The filter and projection operations can effectively remove the blurriness and control the minimum length scale in the derived pattern of the secondary structures (Sigmund and Maute 2013). The surface-PDE filter for the design variable γ is

$$
\begin{cases}
-\nabla_s \cdot \left(r_f^2 \nabla_s \gamma_f \right) + \gamma_f = \gamma, \text{ on } \Sigma \\
\gamma_f = 0, \text{ at } \partial\Sigma
\end{cases}, \tag{17}
$$

where r_f is the filter radius, which is constant. The filtered design variable γ_f is projected to derive the material density:

$$
\gamma_p = \frac{\tanh(\beta\xi) + \tanh(\beta(\gamma_f - \xi))}{\tanh(\beta\xi) + \tanh(\beta(1 - \xi))}, \tag{18}
$$

where β and ξ are the parameters for this threshold projection, with values chosen based on numerical experiments (Guest et al. 2004). The surface-PDE filter, the threshold projection, and the related quantities are sketched in Fig. 6.

2.2.3 Coupling of design variables

In this topology optimization, the design variable of the secondary structures is defined on the 2-manifold described by the design variable for the external surface of the base structure. The design variable for the external surface of the base structure implicitly describes a variable design domain of the secondary structures. During the optimization process, the two design variables are coupled, because the surface gradient operator ∇_s defined on the implicitly described 2-manifold Σ requires to be transformed into its equivalent form defined on Ω.

Because the 2-manifold Σ is the graph of a function defined on Ω, Σ is homeomorphic to Ω, and the function in $\mathcal{H}(\Sigma)$ can be transformed into its equivalent form in $\mathcal{H}(\Omega)$, where $\mathcal{H}(\Sigma)$ and $\mathcal{H}(\Omega)$ are the first-order Sobolev spaces defined on Σ and Ω, respectively. This transformation can be implemented by replacing the independent variable $\mathbf{x}_\Sigma$ of the function in $\mathcal{H}(\Sigma)$ with $\mathbf{x}_\Omega + z_s(\mathbf{x}_\Omega)\mathbf{k}$. Therefore, $\mathcal{H}(\Sigma)$ is homeomorphic to $\mathcal{H}(\Omega)$, and the function in $\mathcal{H}(\Sigma)$ and its equivalent counterpart in $\mathcal{H}(\Omega)$ are not distinguished in this paper. The surface gradient operator ∇_s defined on Σ can be transformed into its equivalent form $\nabla - [\mathbf{n}_s(z_s) \cdot \nabla]\mathbf{n}_s(z_s)$ defined on Ω:

$$
\nabla_s = \nabla - \frac{\nabla z_s - \mathbf{k}}{1 + |\nabla z_s|^2}(\nabla z_s \cdot \nabla), \tag{19}
$$

where $\mathbf{n}_s(z_s)$, sketched in Fig. 5, is the unitary normal vector of Σ, and it is expressed as

$$
\mathbf{n}_s(z_s) = \frac{-\nabla z_s + \mathbf{k}}{\sqrt{1 + |\nabla z_s|^2}}. \tag{20}
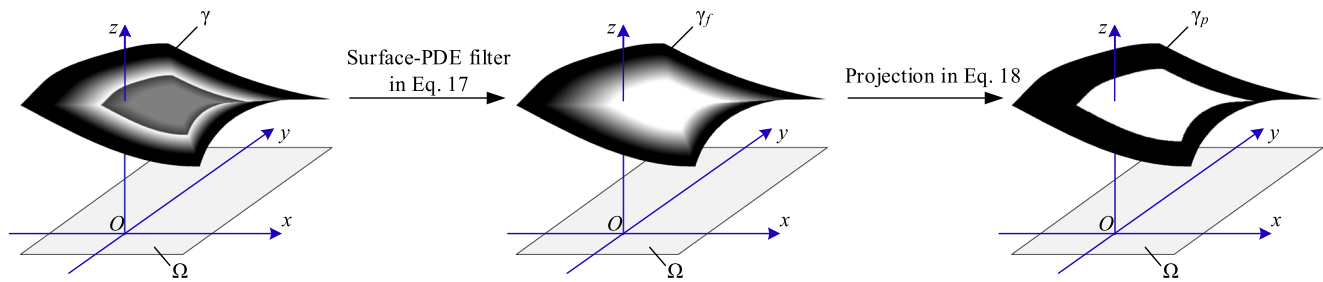$$

Fig. 6 Sketch for the surface-PDE filter and threshold projection of the design variable of the secondary structures. In this sketch, γ is the design variable of the secondary structures; γ_f and γ_p are the filtered and projected counterparts of γ, respectively

Because ∇_s depends on z_s, its first-order variational to z_s is:

$$\nabla_s^{(\tilde{z}_s)} = -\frac{\nabla z_s - \mathbf{k}}{1 + |\nabla z_s|^2} (\nabla \tilde{z}_s \cdot \nabla) - \frac{\nabla \tilde{z}_s}{1 + |\nabla z_s|^2} (\nabla z_s \cdot \nabla)$$
$$+ \frac{2(\nabla z_s - \mathbf{k})}{(1 + |\nabla z_s|^2)^2} (\nabla z_s \cdot \nabla \tilde{z}_s)(\nabla z_s \cdot \nabla),$$
$$\forall \tilde{z}_s \in \mathcal{H}(\Omega) \tag{21}$$

where $\tilde{z}_s$ is the test function of z_s; the superscript $(\tilde{z}_s)$ is used to indicate the dependence on $\tilde{z}_s$. The first-order variational of ∇_s to z_s will be used in the adjoint analysis of the topology optimization problem.

After the implementation of the topology optimization, the match between the external surface of the base structure and the pattern of the secondary structures can be optimized, where the ordinate distribution z_s on Σ converges to the outer shape of the base structure and the material density γ_p is penalized into the pattern of the secondary structures. By defining the natural projection $proj_1 : \Sigma \times \gamma_p(\Sigma) \to \Sigma$ satisfying

$$proj_1(\varphi(\mathbf{x}_\Sigma), \gamma_p(\mathbf{x}_\Sigma)) = \mathbf{x}_\Omega \text{ for } \forall \mathbf{x}_\Sigma \in \Sigma, \tag{22}$$

the optimized match between the external surface of the base structure and pattern of the secondary structures composes the fiber bundle:

$$(\Sigma \times \gamma_p(\Sigma), \Sigma, proj_1, \gamma_p(\Sigma)), \tag{23}$$

where Σ and $\gamma_p : \Sigma \to [0, 1]$ are the base manifold and the fibers of this fiber bundle, respectively; φ is the homeomorphism determined by the bijection $\mathbf{x}_\Sigma = \mathbf{x}_\Omega + z_s(\mathbf{x}_\Omega)\mathbf{k}$. Therefore, topology optimization of the fiber bundle in (23) can be implemented by optimizing the match between its base manifold and fibers, where the optimization process is implemented on a variable design domain evolving together with the structures defined on it.

Based on the transformation of the base pressure in (16) and the transformed surface gradient operator in (19), the dimensionless Young-Laplace equation in (11) can be transformed into the following form, which is used to describe the two-phase interfaces on the fiber bundle described in (23):

$$\begin{cases} \begin{cases} \nabla_s \cdot \left[\bar{\sigma}(\gamma_p) \frac{\nabla_s \bar{d}}{\sqrt{1/d_0^2 + |\nabla_s \bar{d}|^2}} \right] = 1 - p_\kappa(\gamma_p)\kappa(z_s, z_f), \text{ on } \Sigma(\Omega) \\ \bar{d} = 0, \text{ at } \partial\Sigma(\Omega) \end{cases} \\ \kappa(z_s, z_f) = \frac{\bar{\sigma}_l}{r_m^2} \frac{z_s - b_z z_f}{\left(\sqrt{1 + |\nabla z_s|^2}\right)^3}, \text{ in } \Omega \\ \bar{\sigma}(\gamma_p) = \bar{\sigma}_l + (\bar{\sigma}_s - \bar{\sigma}_l) q \frac{1 - \gamma_p}{q + \gamma_p} \\ p_\kappa(\gamma_p) = p_{\kappa,\max} + (p_{\kappa,\min} - p_{\kappa,\max}) q \frac{1 - \gamma_p}{q + \gamma_p} \end{cases} \tag{24}$$

2.3 Topology optimization problem

The ratio of the pattern area of the secondary structures to the area of the external surface of the base structure is referred to as the duty ratio, which is a key factor used to retrieve the macroscale wetting performance of hierarchial microtextures. The duty ratio can be computed as $|\mathcal{N}|/|\Sigma|$, where $|\mathcal{N}|$ and $|\Sigma|$ represent the areas of $\mathcal{N}$ and

Σ sketched in Fig. 3, respectively. To derive the hierarchical microtextures with a specified value of the duty ratio, a bilateral constraint on the duty ratio of the fiber bundle can be added to the topology optimization problem of the hierarchical microtextures.

The optimization task is to find the fiber bundle for the hierarchical microtextures with a specified duty ratio, by equivalently minimizing the volume of the liquid bulges

suspended at the liquid/vapor interface in the terminal state of the Cassie-Baxter mode, where the fiber bundle is composed of the 2-manifold and fibers corresponding to the external

surface of the base structure and the pattern of the secondary structures, respectively. Therefore, the corresponding topology optimization problem can be formulated as
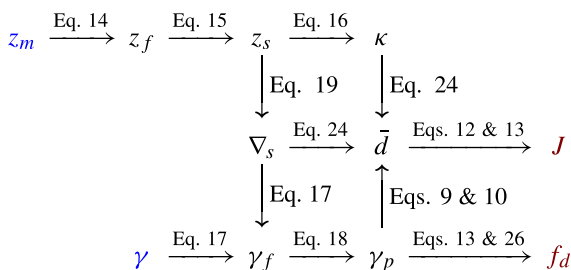
$$
\begin{aligned}
&\text{find } z_m : \Omega \mapsto [0, 1] \text{ and } \gamma : \Sigma \mapsto [0, 1] \text{ for } \left(\Sigma \times \gamma_p\left(\Sigma\right), \Sigma, proj_1, \gamma_p\left(\Sigma\right)\right), \\
&\text{to minimize } \frac{J}{J_0} \text{ with } J = \frac{1}{|\Sigma|^2} \int_\Sigma \bar{d}^2 \, d\Sigma \text{ constrained by}
\end{aligned}
$$

$$
\begin{cases}
\begin{cases}
\begin{cases}
\nabla_s \cdot \left[\bar{\sigma}\left(\gamma_p\right) \dfrac{\nabla_s \bar{d}}{\sqrt{1/d_0^2 + |\nabla_s \bar{d}|^2}}\right] = 1 - p_\kappa\left(\gamma_p\right) \kappa\left(z_s, z_f\right), \text{ on } \Sigma\left(\Omega\right) \\
\bar{d} = 0, \text{ at } \partial\Sigma\left(\Omega\right) \\
\kappa\left(z_s, z_f\right) = \dfrac{\bar{\sigma}_l}{r_m^2} \dfrac{z_s - b_z z_f}{\left(\sqrt{1 + |\nabla z_s|^2}\right)^3}, \text{ in } \Omega \\
\bar{\sigma}\left(\gamma_p\right) = \bar{\sigma}_l + \left(\bar{\sigma}_s - \bar{\sigma}_l\right) q \frac{1-\gamma_p}{q+\gamma_p} \\
p_\kappa\left(\gamma_p\right) = p_{\kappa,\max} + \left(p_{\kappa,\min} - p_{\kappa,\max}\right) q \frac{1-\gamma_p}{q+\gamma_p}
\end{cases} \\
\begin{cases}
-\nabla \cdot \left(r_m^2 \nabla z_f\right) + z_f = z_m, \text{ in } \Omega \quad \text{(PDE filter 1)} \\
z_f = 0, \text{ on } \partial\Omega
\end{cases} \\
\begin{cases}
-\nabla \cdot \left(r_m^2 \nabla z_s\right) + z_s = b_z z_f, \text{ in } \Omega \quad \text{(PDE filter 2)} \\
z_s = 0, \text{ on } \partial\Omega
\end{cases} \\
\begin{cases}
-\nabla_s \cdot \left(r_f^2 \nabla_s \gamma_f\right) + \gamma_f = \gamma, \text{ on } \Sigma\left(\Omega\right) \quad \text{(PDE filter 3)} \\
\gamma_f = 0, \text{ at } \partial\Sigma\left(\Omega\right)
\end{cases} \\
\gamma_p = \frac{\tanh(\beta\xi) + \tanh(\beta(\gamma_f - \xi))}{\tanh(\beta\xi) + \tanh(\beta(1-\xi))} \quad \text{(Threshold projection)} \\
|f_d - f_0| \leq 10^{-3} \quad \text{(Duty-ratio constraint)}
\end{cases}
$$

(Young − Laplace equation) , (25)

where J_0 is the value of the performance measurement corresponding to the initial distributions of the design variables z_m and γ; f_d is the duty ratio expressed as

$$
f_d = \frac{1}{|\Sigma|} \int_\Sigma 1 - \gamma_p \, d\Sigma; \tag{26}
$$

and $f_0 \in (0, 1)$ is the specified duty ratio with a permitted tolerance of 10^{-3}.

The coupling relations among the variables, functions, and surface gradient operator in the topology optimization problem are illustrated by the following arrow chart:

$$
\begin{array}{ccccccc}
z_m & \xrightarrow{\text{Eq. 14}} & z_f & \xrightarrow{\text{Eq. 15}} & z_s & \xrightarrow{\text{Eq. 16}} & \kappa \\
& & & & \downarrow{\scriptstyle\text{Eq. 19}} & & \downarrow{\scriptstyle\text{Eq. 24}} \\
& & & & \nabla_s & \xrightarrow{\text{Eq. 24}} & \bar{d} \xrightarrow{\text{Eqs. 12 \& 13}} J \\
& & & & \downarrow{\scriptstyle\text{Eq. 17}} & & \uparrow{\scriptstyle\text{Eqs. 9 \& 10}} \\
& & \gamma & \xrightarrow{\text{Eq. 17}} & \gamma_f & \xrightarrow{\text{Eq. 18}} & \gamma_p \xrightarrow{\text{Eqs. 13 \& 26}} f_d
\end{array}
$$

where the design variables z_m and γ, marked in blue, are the inputs; the design objective J and the duty ratio f_d, marked in red, are the outputs.

2.4 Adjoint analysis

The topology optimization problem in (25) can be solved by using a gradient-information-based iterative procedure, where the adjoint sensitivities are used to determine the gradient information. An adjoint analysis has been implemented for the performance measurement and the duty ratio to derive their adjoint sensitivities. The details of this adjoint analysis are provided in Appendix Sections 1–4.

Based on the adjoint analysis method (Hinze et al. 2009), the adjoint sensitivity of the performance measurement $J = \frac{1}{|\Sigma|^2} \int_\Sigma \bar{d}^2 \, d\Sigma$ can be computed as

$$
\delta J = \delta\left(\frac{J|\Sigma|^2}{|\Sigma|^2}\right) = \frac{1}{|\Sigma|^2}\delta\left(J|\Sigma|^2\right) - \frac{2J}{|\Sigma|}\delta|\Sigma|, \tag{27}
$$

where δ is the first-order variational operator. In (27), the adjoint sensitivity of $J|\Sigma|^2 = \int_\Sigma \bar{d}^2 \, d\Sigma$ is derived as

$$
\delta\left(J|\Sigma|^2\right) = -\int_\Sigma \gamma_{fa}\delta\gamma \, d\Sigma - \int_\Omega z_{fa}\delta z_m \, d\Omega,
$$
$$
\delta\gamma \in \mathcal{H}^{-1}\left(\Sigma\right) \text{ and } \delta z_m \in \mathcal{H}^{-1}\left(\Omega\right), \tag{28}
$$

where γ_{fa} and z_{fa} are the adjoint variables of the filtered design variables γ_f and z_f, respectively; being similar with $\mathcal{H}^{-1}\left(\Omega\right)$, $\mathcal{H}^{-1}\left(\Sigma\right)$ is the dual space of $\overset{\circ}{\mathcal{H}}\left(\Sigma\right)$ representing

the closure of the compactly supported and infinitely smooth function space $C_0^\infty(\Sigma)$. In (27), γ_{fa} and z_{fa} are derived by sequentially solving the following variational formulations of the adjoint equations:

– Find $\bar{d}_a \in \mathcal{H}(\Sigma)$ with $\bar{d}_a = 0$ at $\partial\Sigma$, satisfying

$$\int_\Sigma 2\bar{d}\tilde{\bar{d}} - \bar{\sigma}\frac{\nabla_s \bar{d}_a \cdot \nabla_s \tilde{\bar{d}}}{\sqrt{1/d_0^2 + |\nabla_s \bar{d}|^2}}$$
$$+\bar{\sigma}\frac{\left(\nabla_s \bar{d} \cdot \nabla_s \bar{d}_a\right)\left(\nabla_s \bar{d} \cdot \nabla_s \tilde{\bar{d}}\right)}{\left(\sqrt{1/d_0^2 + |\nabla_s \bar{d}|^2}\right)^3}\,\mathrm{d}\Sigma = 0,$$
$$\forall \tilde{\bar{d}} \in \mathcal{H}(\Sigma); \tag{29}$$

– Find $\kappa_a \in \overset{\circ}{\mathcal{H}}(\Omega)$, satisfying

$$\int_\Omega \left(p_\kappa \bar{d}_a \sqrt{1 + |\nabla z_s|^2} + \kappa_a\right)\tilde{\kappa}_a\,\mathrm{d}\Omega = 0,\ \forall \tilde{\kappa}_a \in \mathcal{H}^{-1}(\Omega); \tag{30}$$

– Find $\gamma_{fa} \in \mathcal{H}(\Sigma)$ with $\gamma_{fa} = 0$ at $\partial\Sigma$, satisfying

$$\int_\Sigma r_f^2 \nabla_s \gamma_{fa} \cdot \nabla_s \tilde{\gamma}_{fa} + \gamma_{fa}\tilde{\gamma}_{fa} - \frac{\partial\bar{\sigma}}{\partial\gamma_p}\frac{\partial\gamma_p}{\partial\gamma_f}$$
$$\times \frac{\nabla_s \bar{d} \cdot \nabla_s \bar{d}_a}{\sqrt{1/d_0^2 + |\nabla_s \bar{d}|^2}}\tilde{\gamma}_{fa} + \frac{\partial p_\kappa}{\partial\gamma_p}\frac{\partial\gamma_p}{\partial\gamma_f}\kappa \bar{d}_a\tilde{\gamma}_{fa}\,\mathrm{d}\Sigma = 0,$$
$$\forall \tilde{\gamma}_{fa} \in \mathcal{H}(\Sigma); \tag{31}$$

– Find $z_{sa} \in \mathcal{H}(\Omega)$ with $z_{sa} = 0$ on $\partial\Omega$, satisfying

$$\int_\Omega r_m^2 \nabla z_{sa} \cdot \nabla\tilde{z}_{sa} + z_{sa}\tilde{z}_{sa} + r_f^2$$
$$\times \left[\nabla_s^{(\tilde{z}_{sa})}\gamma_f \cdot \nabla_s \gamma_{fa} + \nabla_s \gamma_f \cdot \nabla_s^{(\tilde{z}_{sa})}\gamma_{fa}\right]\sqrt{1 + |\nabla z_s|^2}$$
$$-\bar{\sigma}\left[\frac{\nabla_s^{(\tilde{z}_{sa})}\bar{d} \cdot \nabla_s \bar{d}_a + \nabla_s \bar{d} \cdot \nabla_s^{(\tilde{z}_{sa})}\bar{d}_a}{\sqrt{1/d_0^2 + |\nabla_s \bar{d}|^2}}\right.$$
$$\left.-\frac{\left(\nabla_s \bar{d} \cdot \nabla_s \bar{d}_a\right)\left(\nabla_s^{(\tilde{z}_{sa})}\bar{d} \cdot \nabla_s \bar{d}\right)}{\left(\sqrt{1/d_0^2 + |\nabla_s \bar{d}|^2}\right)^3}\right]\sqrt{1 + |\nabla z_s|^2}$$
$$+\left[\bar{d}^2 - \bar{\sigma}\frac{\nabla_s \bar{d} \cdot \nabla_s \bar{d}_a}{\sqrt{1/d_0^2 + |\nabla_s \bar{d}|^2}} - (1 - p_\kappa\kappa)\bar{d}_a + r_f^2\nabla_s \gamma_f\right.$$
$$\left.\cdot\nabla_s \gamma_{fa} + \gamma_f\gamma_{fa} - \gamma\gamma_{fa}\right]\frac{\nabla z_s \cdot \nabla\tilde{z}_{sa}}{\sqrt{1 + |\nabla z_s|^2}}$$
$$-\frac{\bar{\sigma}_l}{r_m^2}\left[\frac{\tilde{z}_{sa}}{\left(\sqrt{1 + |\nabla z_s|^2}\right)^3} - 3\frac{(z_s - b_z z_f)(\nabla z_s \cdot \nabla\tilde{z}_{sa})}{\left(\sqrt{1 + |\nabla z_s|^2}\right)^5}\right]$$
$$\times\kappa_a\,\mathrm{d}\Omega = 0,\ \forall\tilde{z}_{sa} \in \mathcal{H}(\Omega); \tag{32}$$

– Find $z_{fa} \in \mathcal{H}(\Omega)$ with $z_{fa} = 0$ on $\partial\Omega$, satisfying

$$\int_\Omega r_m^2 \nabla z_{fa} \cdot \nabla\tilde{z}_{fa} + z_{fa}\tilde{z}_{fa} - b_z z_{sa}\tilde{z}_{fa}$$
$$+\frac{\bar{\sigma}_l}{r_m^2}\frac{b_z\kappa_a}{\left(\sqrt{1 + |\nabla z_s|^2}\right)^3}\tilde{z}_{fa}\,\mathrm{d}\Omega = 0,\ \forall\tilde{z}_{fa} \in \mathcal{H}(\Omega), \tag{33}$$

where $\bar{d}_a$, κ_a, and z_{sa} are the adjoint variables of $\bar{d}$, κ, and z_s, respectively; $\tilde{\bar{d}}_a$, $\tilde{\kappa}_a$, $\tilde{\gamma}_a$, $\tilde{z}_{sa}$, and $\tilde{z}_{fa}$ are the test functions of the adjoint variables $\bar{d}_a$, κ_a, γ_a, z_{sa}, and z_{fa}, respectively. The adjoint sensitivity of the area of Σ in (27) is derived as

$$\delta|\Sigma| = -\int_\Omega z_{fa}\delta z_m\,\mathrm{d}\Omega,\ \delta z_m \in \mathcal{H}^{-1}(\Omega), \tag{34}$$

where the adjoint variable z_{fa} is derived by sequentially solving the following variational formulations of the adjoint equations:

– Find $z_{sa} \in \mathcal{H}(\Omega)$ with $z_{sa} = 0$ on $\partial\Omega$, satisfying

$$\int_\Omega \frac{\nabla z_s \cdot \nabla\tilde{z}_{sa}}{\sqrt{1 + |\nabla z_s|^2}} + r_m^2\nabla z_{sa} \cdot \nabla\tilde{z}_{sa} + z_{sa}\tilde{z}_{sa}\,\mathrm{d}\Omega = 0,$$
$$\forall\tilde{z}_{sa} \in \mathcal{H}(\Omega); \tag{35}$$

– Find $z_{fa} \in \mathcal{H}(\Omega)$ with $z_{fa} = 0$ on $\partial\Omega$, satisfying

$$\int_\Omega r_m^2\nabla z_{fa} \cdot \nabla\tilde{z}_{fa} + z_{fa}\tilde{z}_{fa} - b_z z_{sa}\tilde{z}_{fa}\,\mathrm{d}\Omega = 0,$$
$$\forall\tilde{z}_{fa} \in \mathcal{H}(\Omega). \tag{36}$$

For the constraint of the duty ratio, the adjoint sensitivity of the duty ratio can be derived from that of $f_d|\Sigma|$ and $|\Sigma|$:

$$\delta f_d = \delta\left(\frac{f_d|\Sigma|}{|\Sigma|}\right) = \frac{1}{|\Sigma|}\delta(f_d|\Sigma|) - \frac{f_d}{|\Sigma|}\delta|\Sigma|. \tag{37}$$

In (37), the adjoint sensitivity of $|\Sigma|$ is derived from (34), where the adjoint variables are solved from (35) and (36); the adjoint sensitivity of the pattern area $f_d|\Sigma| = \int_\Sigma 1 - \gamma_p\,\mathrm{d}\Sigma$ of the secondary structures is derived as

$$\delta(f_d|\Sigma|) = -\int_\Sigma \gamma_{fa}\delta\gamma\,\mathrm{d}\Sigma - \int_\Omega z_{fa}\delta z_m\,\mathrm{d}\Omega,$$
$$\delta\gamma \in \mathcal{H}^{-1}(\Sigma)\text{ and }\delta z_m \in \mathcal{H}^{-1}(\Omega), \tag{38}$$

where the adjoint variables γ_{fa} and z_{fa} are solved from the following variational formulations of the adjoint equations:

– Find $\gamma_{fa} \in \mathcal{H}(\Sigma)$ with $\gamma_{fa} = 0$ at $\partial\Sigma$, satisfying

$$\int_\Sigma -\frac{\partial\gamma_p}{\partial\gamma_f}\tilde{\gamma}_{fa} + r_f^2\nabla_s \gamma_{fa} \cdot \nabla_s \tilde{\gamma}_{fa} + \gamma_{fa}\tilde{\gamma}_{fa}\,\mathrm{d}\Sigma = 0,$$
$$\forall\tilde{\gamma}_{fa} \in \mathcal{H}(\Sigma); \tag{39}$$

– Find $z_{sa} \in \mathcal{H}(\Omega)$ with $z_{sa} = 0$ at $\partial\Omega$, satisfying

$$
\int_\Omega r_f^2 \left(\nabla_s^{(\tilde{z}_{sa})} \gamma_f \cdot \nabla_s \gamma_{fa} + \nabla_s \gamma_f \cdot \nabla_s^{(\tilde{z}_{sa})} \gamma_{fa} \right)
$$
$$
\times \sqrt{1 + |\nabla z_s|^2} + \left(1 - \gamma_p + r_f^2 \nabla_s \gamma_f \cdot \nabla_s \gamma_{fa} \right.
$$
$$
\left. + \gamma_f \gamma_{fa} - \gamma \gamma_{fa} \right) \frac{\nabla z_s \cdot \nabla \tilde{z}_{sa}}{\sqrt{1 + |\nabla z_s|^2}}
$$
$$
+ r_m^2 \nabla z_{sa} \cdot \nabla \tilde{z}_{sa} + z_{sa} \tilde{z}_{sa} \, \mathrm{d}\Omega = 0, \ \forall \tilde{z}_{sa} \in \mathcal{H}(\Omega);
$$
(40)

– Find $z_{fa} \in \mathcal{H}(\Omega)$ with $z_{fa} = 0$ at $\partial\Omega$, satisfying

$$
\int_\Omega r_m^2 \nabla z_{fa} \cdot \nabla \tilde{z}_{fa} + z_{fa} \tilde{z}_{fa} - b_z z_{sa} \tilde{z}_{fa} \, \mathrm{d}\Omega = 0,
$$
$$
\forall \tilde{z}_{fa} \in \mathcal{H}(\Omega).
$$
(41)

After the derivation of the adjoint sensitivities in (27) and (37), the design variables z_m and γ can be iteratively evolved to obtain the fiber bundle for the hierarchical microtextures.

2.5 Numerical implementation

To solve the topology optimization problem in (25), an optimization procedure is implemented as outlined by the pseudocode in Table 1. The finite element method is utilized to solve the variational formulations of the PDEs (Appendix Section 1) and adjoint equations. The finite element solution can be obtained using a finite element software package that includes a nonlinear solver. The dimensionless counterparts of the lattices used to tile a solid surface are discretized by using the triangular elements with a size of 1/120 (Fig. 7). Linear elements are used to discretize the design domains, because a relative fine mesh with linear elements can simultaneously enhance the efficiency of the numerical implementation and ensure the numerical accuracy of the finite element solution. Linear elements can also effectively ensure the positivity of the distributions of the design variables, filtered design variables, and material density.

In the iterative procedure, the projection parameter β, with the initial value of 1, is doubled after every 30 iterations; the loop is stopped when the maximal number of iterations is reached or if the averaged variation of the design objective over continuous 5 iterations and the residual of the constraint on the duty ratio are simultaneously less than the specified tolerance of 10^{-3}. The design variables are updated by using the method of moving asymptotes (Svanberg 1987).

Table 1 Pseudocode for topology optimization of the fiber bundle for hierarchical microtextures

Choose $\bar{\sigma}_l$, f_0 and d_0;

Set
$\begin{cases} n_{\max} \leftarrow 315 \\ \gamma \leftarrow 1 - f_0 \\ z_m \leftarrow 1 \\ n_i \leftarrow 1 \\ \xi \leftarrow 0.5 \\ \beta \leftarrow 1 \end{cases}$, and
$\begin{cases} \bar{\sigma}_s \leftarrow 10^5 \bar{\sigma}_l \\ q \leftarrow 10^{-4} \\ p_{\kappa,\min} \leftarrow 0 \\ p_{\kappa,\max} \leftarrow 1 \end{cases}$

loop

  Solve (14) to derive z_f by filtering z_m;

  Solve (15) to derive z_s by filtering z_f;

  Solve (17) to derive γ_f by filtering γ;

  Project γ_f to derive γ_p and compute f_d;

  Solve $\bar{d}$ and κ from (24), and evaluate J/J_0 from (12);

  Solve $\bar{d}_a$, κ_a, γ_{fa}, z_{sa}, and z_{fa} from (29–33);

  Evaluate $\delta\left(J/|\Sigma|^2\right)$ from (28);

  Solve z_{sa} and z_{fa} from (35) and (36);

  Evaluate $\delta|\Sigma|$ from (34);

  Calculate δJ from (27) based on $\delta\left(J/|\Sigma|^2\right)$ and $\delta|\Sigma|$;

  Solve γ_{fa}, z_{sa}, and z_{fa} from (39)–(41);

  Evaluate $\delta(f_d|\Sigma|)$ from (38);

  Calculate δf_d in (37) from $\delta(f_d|\Sigma|)$ and $\delta|\Sigma|$;

  Update z_m and γ, based on $\delta J/J_0$ and δf_d;

  if mod $(n_i, 30) == 0$

    $\beta \leftarrow 2\beta$;

  end(if)

  if $(n_i == n_{\max})$ or $\begin{cases} \beta == 2^{10} \\ \frac{1}{5}\sum_{m=0}^4 \left| J_{n_i} - J_{n_i - m} \right| \big/ J_0 \le 10^{-3} \\ |f_d - f_0| \le 10^{-3} \end{cases}$

    break;

  end(if)

  $n_i \leftarrow n_i + 1$

end(loop)

In the iterative solution loop for the topology optimization problem in (25), n_i is the loop-index, $n_{\max}$ is the maximal value of n_i, J_{n_i} is the value of J in the n_ith iteration, and mod is the operator used to take the remainder

3 Results and discussion

In this section, various hierarchical microtextures are numerically investigated for their wetting behaviors in the Cassie-Baxter mode. They are designed using the approach introduced in Section 2, with the design parameters listed in Table 2. Based on the optimization procedure, a fiber bundle can be firstly derived by solving the topology optimization problem with a reasonable choice of the parameters. Then, the derived result can be translated into a manufacturable design by applying offset and scaling operations to it (Fig. 3).
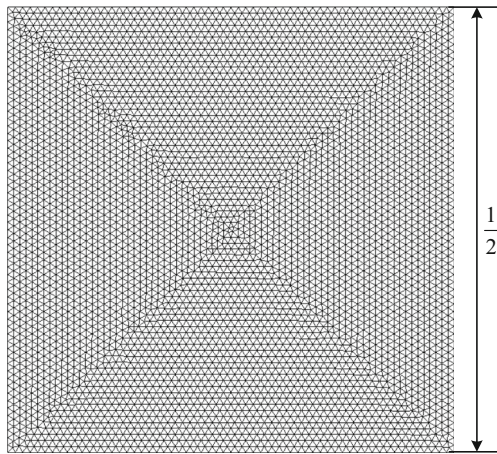
Fig. 7 Illustration for a finite element mesh with triangular elements used to discretize the dimensionless design domains

In the offset operation, the offset distance is the key parameter. This parameter can be determined based on the fact that the maximal value of the contact angle at the sidewalls of the secondary structures is not larger than the crucial advancing angle, when the three-phase contact lines are anchored at the corners corresponding to the pattern boundaries of the secondary structures. Therefore, the offset distance satisfies

$$\begin{cases} d_E = d_0 \bar{d}, \ \forall \mathbf{x}_\Sigma \in \mathcal{N} \\ d_E \leq d_0 \left(\inf \bar{d}_c \right), \ \forall \mathbf{x}_\Sigma \in \Sigma \setminus \mathcal{N} \end{cases}, \quad (42)$$

where d_E is the offset distance, inf is the operator used to extract the infimum of a function, $\bar{d}_c$ is the normalized displacement of the critical liquid/vapor interface supported by the secondary structures, and $\mathcal{N}$ is the pattern of the secondary structures. The pattern $\mathcal{N}$ is the null space of $\gamma_p > 1/2$ at the minimum value of the performance measurement:

$$\mathcal{N} = \left\{ \mathbf{x}_\Sigma \in \Sigma : \left(\gamma_p \left(\mathbf{x}_\Sigma \right) \Big|_{\underset{\gamma \in [0,1]}{\arg \min} J} > \frac{1}{2} \right) \in \{0\} \right\}, \quad (43)$$

where $1/2$ is the average of the upper and lower bounds on γ_p. The offset distance d_E and the pattern $\mathcal{N}$ are sketched in Fig. 3. In (42), the critical liquid/vapor interface is determined by using the relation between the contact angle and the critical advancing angle:

$$\sup_{\mathbf{x}_\Sigma \in \partial \mathcal{N}} \theta \left(\mathbf{x}_\Sigma \right) \leq \theta_A, \quad (44)$$

Table 2 Parameters used for solving the topology optimization problem in (25)

$\bar{\sigma}_l$	d_0	r_f	r_m	f_0	z_m	b_z
10^0	10^{-3}	$1/20$	$1/12$	0.3	1	1

where θ and θ_A are the contact angle sketched in Fig. 2b and the critical advancing angle, respectively. The contact angle is expressed as

$$\theta \left(\mathbf{x}_\Sigma \right) = \pi - \cos^{-1} \left(\frac{\nabla \bar{d}}{\left| \nabla \bar{d} \right|} \cdot \mathbf{n}_s \right), \ \forall \mathbf{x}_\Sigma \in \partial \mathcal{N}. \quad (45)$$

For microtextures with known material, the critical advancing angle θ_A is usually found from experimental tests. θ_A is equal to its equilibrium counterpart when the sidewalls are regarded to be smooth and chemically homogeneous; otherwise, it is larger in the hydrophobic case and can be experimentally measured against actual conditions. On more details of the critical advancing angle, one can review the reference of Eral et al. (2013). The normalized displacement $\bar{d}_c$ of the critical liquid/vapor interface corresponding to $\sup_{\mathbf{x}_\Sigma \in \partial \mathcal{N}} \theta \left(\mathbf{x}_\Sigma \right) = \theta_A$ can be determined by using a heuristic bisection procedure similar to that described in the reference of Deng et al. (2019).

After the offset operation, the scaling operation is applied to derive the structural unit. The lattice size is the scaling factor, and it can be found by establishing a suitable compromise between the performance and manufacturability of the hierarchical microtextures. As previously noted, the solution to the dimensionless Young-Laplace equation exhibits a scaling property (Deng et al. 2018, 2019). Based on this property, the liquid/vapor interface supported on the microtextures can be wholly proportionally scaled along with the scaling of the offset fiber bundle. With a smaller lattice size, better performance of the hierarchical microtextures can be realized. However, the selection of a micro-/nanofabrication process physically fixes the feasible minimum feature size of the hierarchical microtextures. Therefore, there is a lower bound on the lattice size, corresponding to a manufacturability constraint, and this lower bound can be determined based on the feasible minimum feature size. On the other hand, because a structural unit derived by scaling an offset fiber bundle should preserve the dominant role of the surface tension, the surface-to-volume ratio of the liquid/vapor interface should be much larger than 1. Therefore, the lattice size should satisfy $L \ll S_c / V_c$, where $S_c = \int_\Sigma \sqrt{1 + d_0^2 \left| \nabla_s \bar{d}_c \right|^2} \, \mathrm{d}\Sigma$ and $V_c = \left| \int_\Sigma d_0 \bar{d}_c \, \mathrm{d}\Sigma \right|$ are the surface area of the critical liquid/vapor interface and the bulk volume of the liquid bulges, respectively.

3.1 Tilings of different symmetry and periodicity

Different tilings of a solid surface can have different symmetries and periodicities, e.g., axial symmetry, radial symmetry, chirality, and quasiperiodicity (Grünbaum and Shephard 2016). In this section, fiber bundles for hierarchical
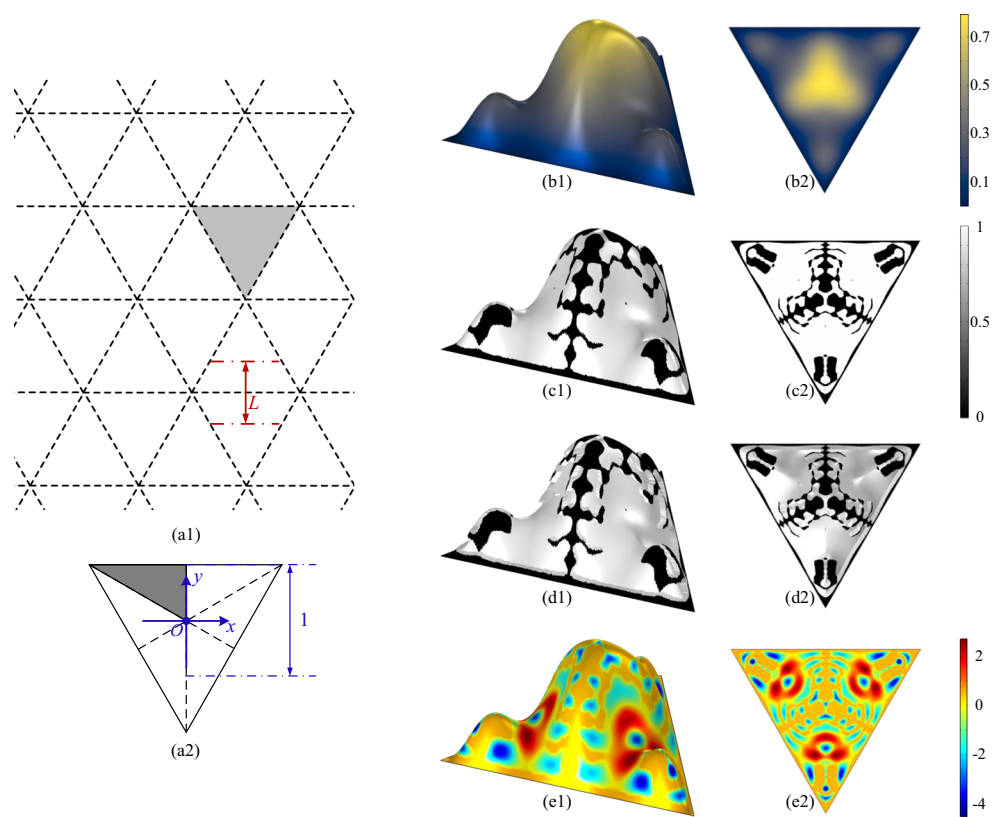
Fig. 8 (a1) Top-view sketch for the regular triangle-based tiling of a flat solid surface. (a2) Irreducible triangular domain of the dimensionless regular-triangle lattice. (b1, b2) Perspective and top views for the external surface of the base structure. (c1, c2) Perspective and top views for the pattern of the secondary structures. (d1, d2) Perspective and top views for the offset fiber bundle. (e1, e2) Perspective and top views for the normalized displacement of the two-phase interfaces relative to the external surface of the base structure

Fig. 9 (a1) Top-view sketch for the regular quadrangle-based tiling of a flat solid surface. (a2) Irreducible triangular domain of the dimensionless regular-quadrangle lattice. (b1, b2) Perspective and top views for the external surface of the base structure. (c1, c2) Perspective and top views for the pattern of the secondary structures. (d1, d2) Perspective and top views for the offset fiber bundle. (e1, e2) Perspective and top views for the normalized displacement of the two-phase interfaces relative to the external surface of the base structure
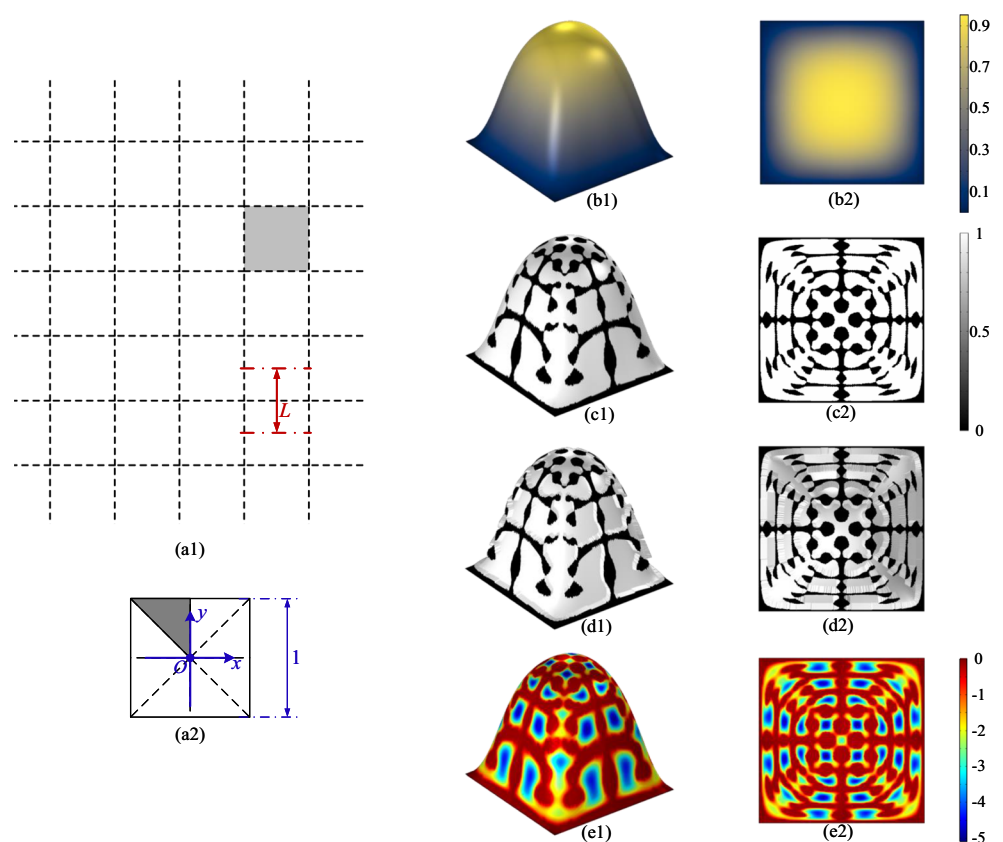
microtextures are derived for the tilings with these symmetries and periodicities.

Axial symmetry is a widely observed geometrical property. Typical periodic tilings with axial symmetry are the ones with regular-polygon lattices, as sketched in Figs. 8a1, 9a1, and 10a1, which show the tilings with regular triangle, quadrangle, and hexagon lattices, respectively. For these periodic tilings, the external surfaces of the base structures and the patterns of the secondary structures, together with the fiber bundles and the normalized displacement of the two-phase interfaces, are derived as shown in Figs. 8b–e, 9b–e, and 10b–e. These results are obtained by solving the optimization problem in (25) on the triangular domains shown in Figs. 8a2, 9a2, and 10a2, which are derived based on the axial symmetry of the regular-polygon lattices. The convergence histories of the iterative solutions and the evolution profiles of the external surfaces and patterns are shown in Fig. 11, from which it can be seen that the convergence processes of the optimization procedure are essentially monotonic. Thus, the convergent performance of the iterative solution procedure can be confirmed. In Fig. 11, local jumps are evident, which are caused by the doubling operation of the projection parameter β in (18).

Radial symmetry of a periodic tiling corresponds to an arrangement of structural units such that two symmetrical halves are produced when the tiling is cut in certain directions through its center. For this symmetry case, the periodic tilings sketched in Figs. 12a1 and 13a1 are considered. The external surfaces of the base structures and the patterns of the secondary structures, together with the fiber bundles and the normalized displacement of the two-phase interfaces, are derived as shown in Figs. 12b–e and 13b–e. These results are obtained by solving the optimization problem in (25) on the triangular domains shown in Figs. 12a2 and 13a2, which are derived based on the axial symmetry of the lattices.

Chirality is an important asymmetry property. A periodic tiling is chiral if it is distinguishable from its mirror image; otherwise, it is achiral. For example, the tilings with axial and radial symmetry in Figs. 8, 9, 10, 12, and 13 are achiral. For the chiral case, the periodic tilings sketched in Figs. 14a1 and 15a1 are considered. The external surfaces of the base structures and the patterns of the secondary structures, together with the fiber bundles and the normalized displacement of the two-phase interfaces, are derived as shown in Figs. 14b–e and 15b–e. These results are obtained by solving the optimization problem in (25) on the whole dimensionless lattices without symmetry-based reduction because of their asymmetry (Figs. 14a2 and 15a2).

Quasiperiodicity is the property characterizing a tiling that displays irregular periodicity. Penrose tiling is a typical example of quasiperiodic tiling generated by using

Fig. 10 (a1) Top-view sketch for the regular hexagon-based tiling of a flat solid surface. (a2) Irreducible triangular-domain of the dimensionless regular-hexagon lattice. (b1, b2) Perspective and top views for the external surface of the base structure. (c1, c2) Perspective and top views for the pattern of the secondary structures. (d1, d2) Perspective and top views for the offset fiber bundle. (e1, e2) Perspective and top views for the normalized displacement of the two-phase interfaces relative to the external surface of the base structure
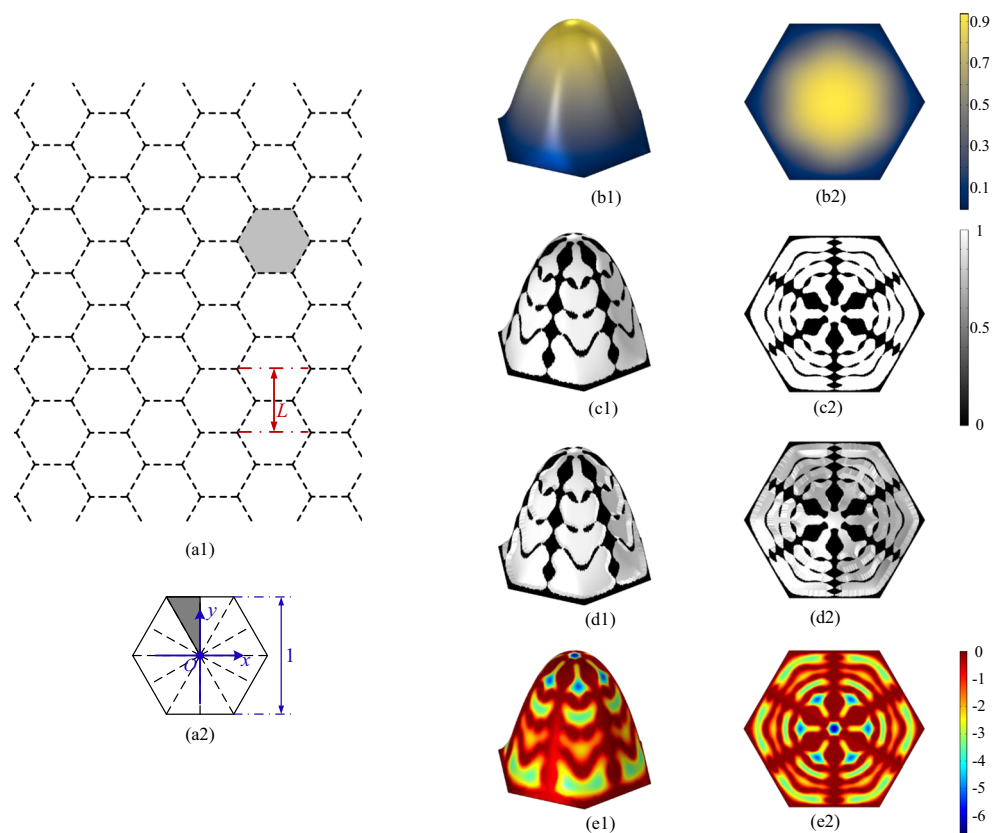
Fig. 11 Convergence histories of the iterative solutions and evolution profiles for the external surface of the base structures and the patterns of the secondary structures on the dimensionless irreducible triangular-domains, for the derived fiber bundles corresponding to the three regular-polygon tilings in Figs. 8a1, 9a1, and 10a1, respectively
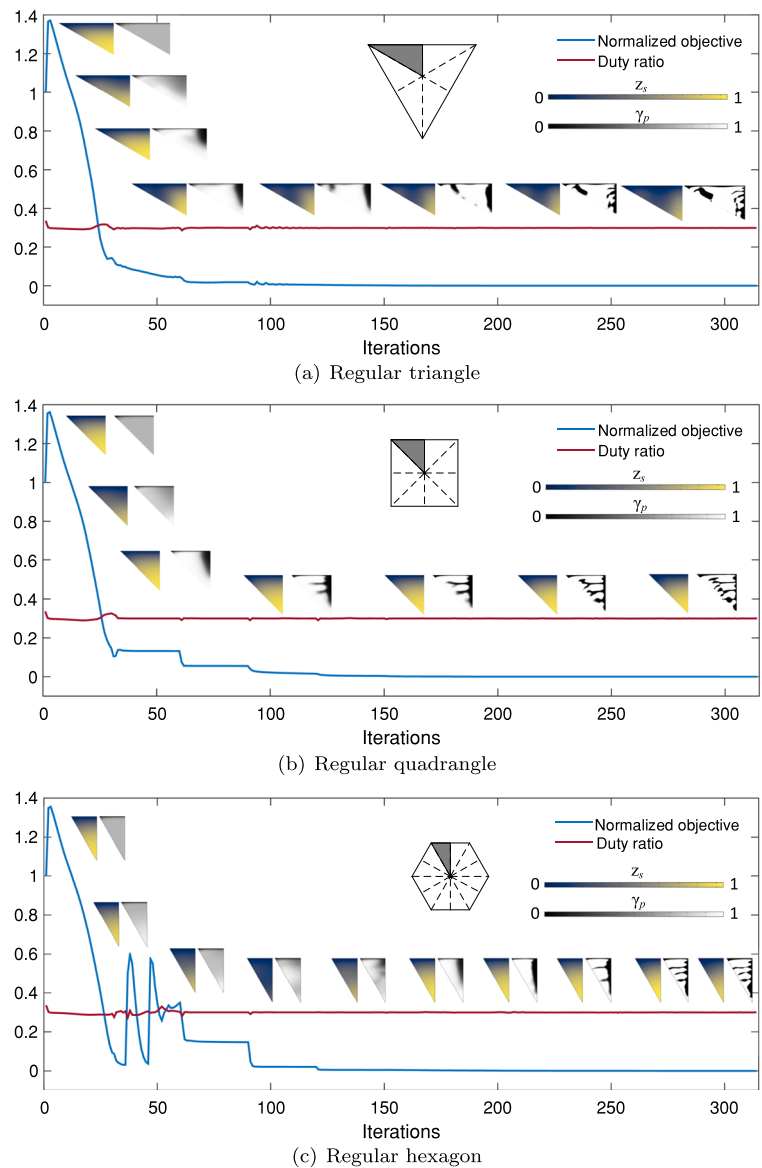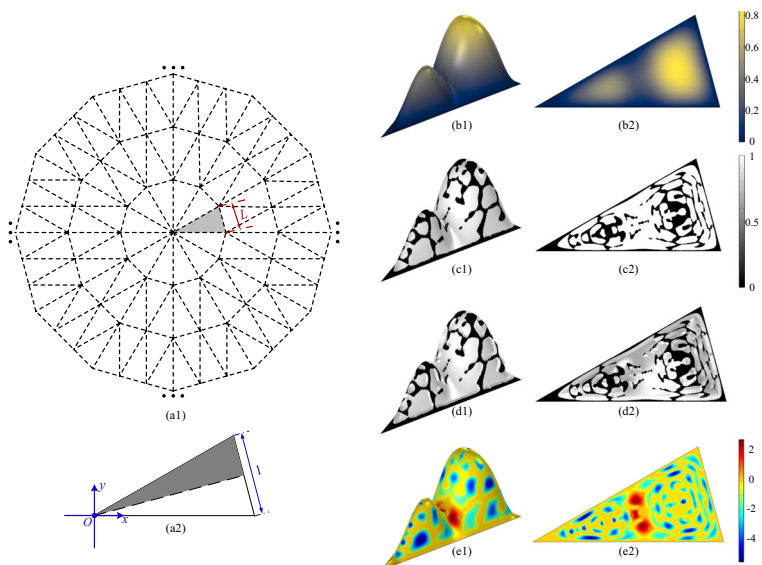

(a) Regular triangle

(b) Regular quadrangle

(c) Regular hexagon

Fig. 12 (a1) Top-view sketch for the radial-symmetry tiling of a flat solid surface, where the tiling lattice is an isosceles triangle with the top angle of 30°. (a2) Irreducible triangular-domain of the dimensionless isosceles-triangle lattice. (b1, b2) Perspective and top views for the external surface of the base structure. (c1, c2) Perspective and top views for the pattern of the secondary structures. (d1, d2) Perspective and top views for the offset fiber bundle. (e1, e2) Perspective and top views for the normalized displacement of the two-phase interfaces relative to the external surface of the base structure

Fig. 13 (a1) Top-view sketch for the radial-symmetry tiling of a flat solid surface, where the tiling lattice is an isosceles triangle with the top angle of 15°. (a2) Irreducible triangular-domain of the dimensionless isosceles-triangle lattice. (b1, b2) Perspective and top views for the external surface of the base structure. (c1, c2) Perspective and top views for the pattern of the secondary structures. (d1, d2) Perspective and top views for the offset fiber bundle. (e1, e2) Perspective and top views for the normalized displacement of the two-phase interfaces relative to the external surface of the base structure
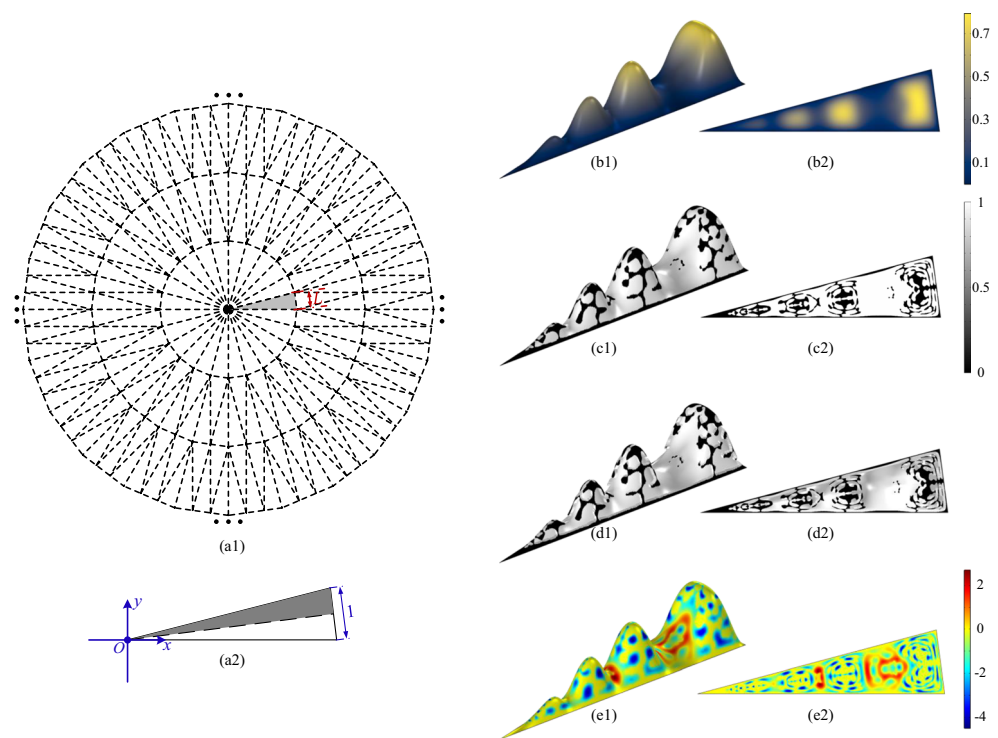
an aperiodic set of prototiles (Grünbaum and Shephard 2016). The typical Penrose tiling sketched in Fig. 16a1 is considered for the case of quasiperiodicity. The external surfaces of the base structures and the patterns of the

secondary structures, together with the fiber bundles and the normalized displacement of the two-phase interfaces, are derived as shown in Fig. 16b–e. These results are obtained by solving the optimization problem in (25) on the two

Fig. 14 (a1) Top-view sketch for the chiral tiling of a flat solid surface, where the tiling lattice is a quadrilateral. (a2) Dimensionless counterpart of the quadrilateral lattice. (b1, b2) Perspective and top views for the external surface of the base structure. (c1, c2) Perspective and top views for the pattern of the secondary structures. (d1, d2) Perspective and top views for the offset fiber bundle. (e1, e2) Perspective and top views for the normalized displacement of the two-phase interfaces relative to the external surface of the base structure
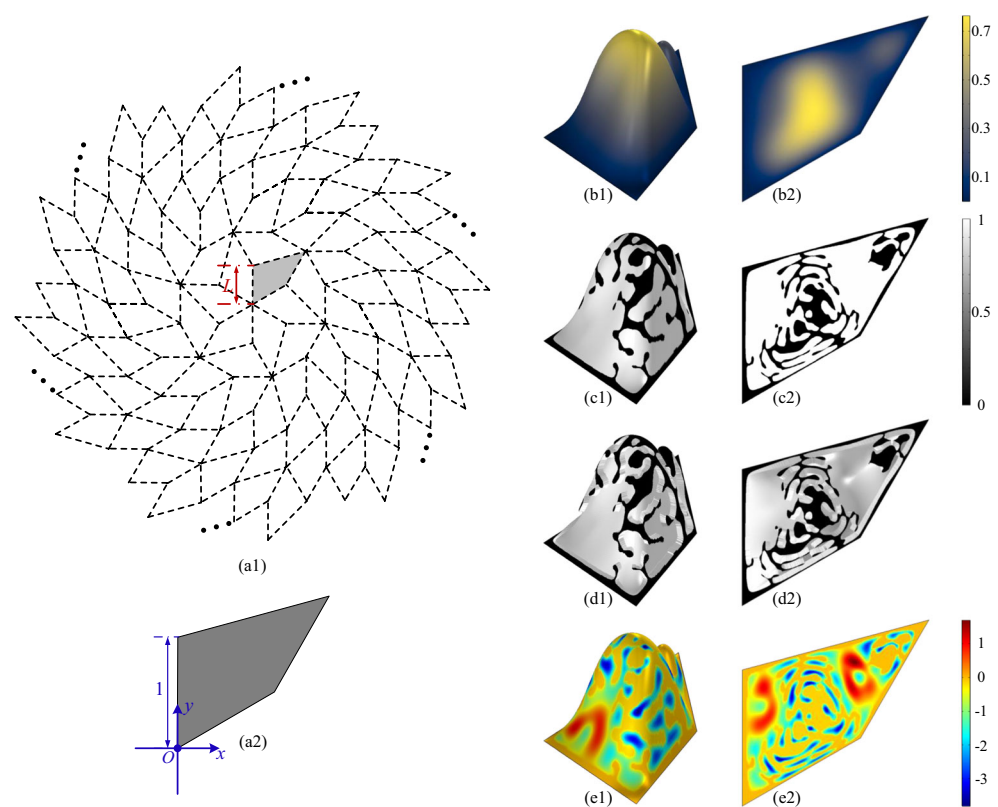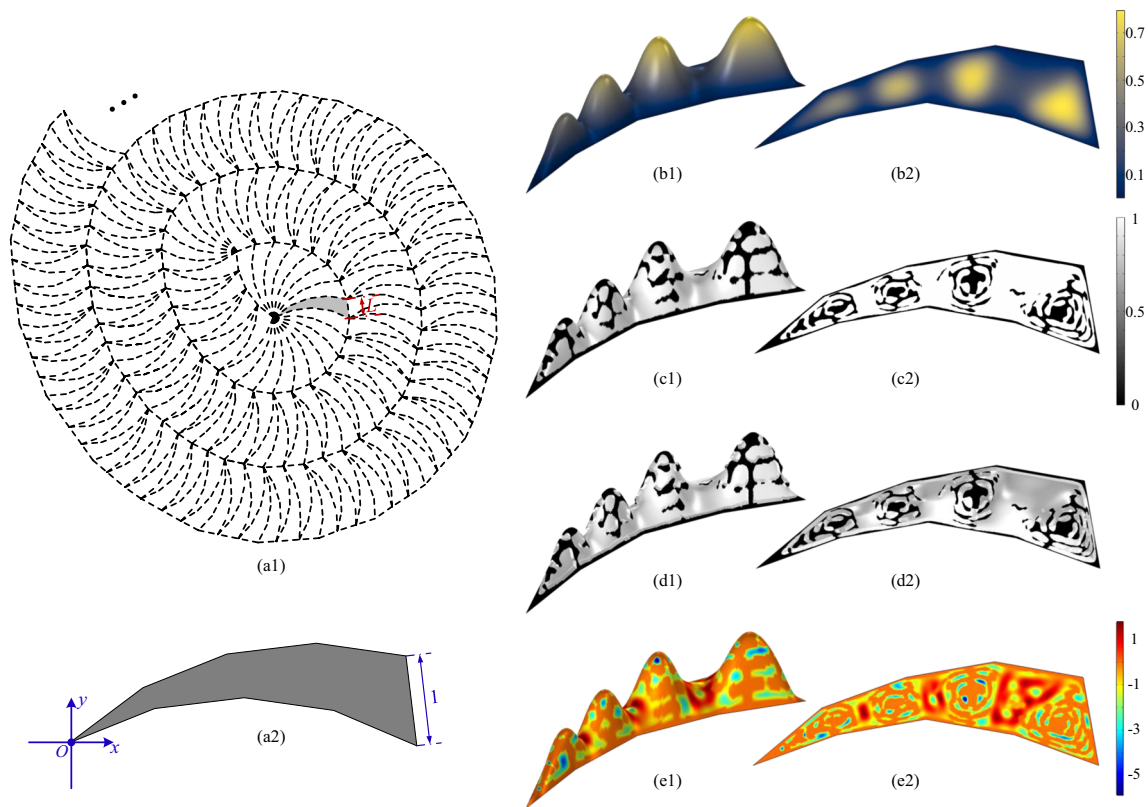
Fig. 15 (a1) Top-view sketch for the chiral tiling of a flat solid surface, where the tiling lattice is a nonagon with equal side-length. (a2) Dimensionless counterpart of the nonagon lattice. (b1, b2) Perspective and top views for the external surface of the base structure. (c1, c2) Perspective and top views for the pattern of the secondary structures. (d1, d2) Perspective and top views for the offset fiber bundle. (e1, e2) Perspective and top views for the normalized displacement of the two-phase interfaces relative to the external surface of the base structure

irreducible triangular domains shown in Figs. 16a2 and 16a3, which are derived based on the axial symmetry of the two rhomboid lattices.

In the fiber bundles derived above, the base structures have peak-like shapes, and most branches of the secondary structures follow the isoheight lines of the base structures. These characteristics can enhance the anchoring stability of the three-phase contact lines and promise more robust metastable states of the Cassie-Baxter mode supported on the derived hierarchical microtextures. The secondary structures are dense and thick around the crests of the peaks of the base structures. This can help to prevent the transitioning of the wetting mode before the terminal state is reached and ensure that the evolution of the liquid/vapor interface follows the process sketched in Fig. 2.

Two or more peaks are prone to arise in the derived external surfaces of the base structures when the tiling lattices have relatively sharp corners, and smaller peaks also tend to arise close to sharper corners. This can be confirmed by comparing Figs. 8b, 12b, 13b, 14b, 15b, and 16b with Figs. 9b and 10b, in which more peaks are formed at sharper corners. When two or more peaks arise, a trough is produced

between every pair of neighboring peaks. The secondary structures tend to lie on the crests instead of the troughs. Troughs have positive curvature and therefore correspond to a positive base pressure. Because troughs tend to lose their ability to support the liquid/vapor interface, as shown by the regions of positive displacement in Figs. 8e, 12e, 13e, 14e, 15e, and 16e, small peaks arise at the sharp corners of the tiling lattice to reduce the trough size of the base structure. The tendency of the secondary structures to lie on the crests of the base structure can ensure that the evolution process sketched in Fig. 2 is followed and provide more support for the liquid/vapor interface.

To study the accuracy of the interpolation schemes, the converged volumes of the liquid bulges suspended at the liquid/vapor interfaces supported by the derived fiber bundles in Figs. 8, 9, and 10 and Figs. 12, 13, 14, 15, and 16 have been compared with their postprocessing counterparts. The postprocessing is implemented by solving the variational formulation of the dimensionless Young-Laplace equation with the normalized displacement of the approximated liquid/solid interface enforced to be zero on a derived pattern of the secondary structures. This zero
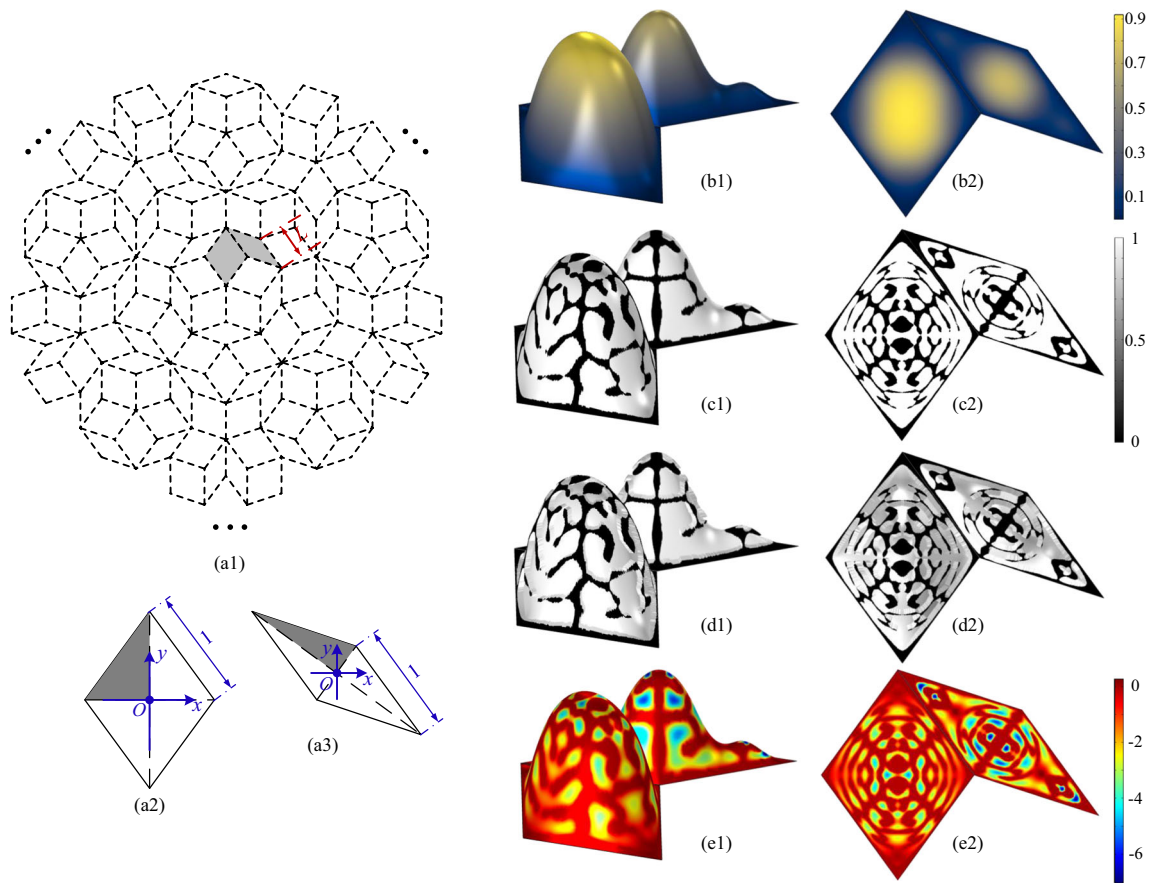
Fig. 16 (a1) Top-view sketch for the Penrose tiling of a flat solid surface, where the tiling lattices are two rhomboids. (a2, a3) Irreducible triangular-domains of the dimensionless rhomboid lattices; (b1, b2) Perspective and top views for the external surface of the base structure. (c1, c2) Perspective and top views for the pattern of the secondary structures. (d1, d2) Perspective and top views for the offset fiber bundle. (e1, e2) Perspective and top views for the normalized displacement of the two-phase interface relative to the external surfaces of the base structure

displacement is imposed by adding the weak constraint $\int_{\mathcal{N}} \bar{d}\tilde{\lambda} + \bar{\tilde{d}}\lambda \, d\Sigma = 0$ to the variational formulation in (54), where λ is the Lagrangian multiplier and $\tilde{\lambda}$ is the test function of λ. The accuracy of the derived fiber bundles is evaluated by the relative tolerance computed as $|V_c - V_p|/V_p$, where V_c and V_p are the volumes of the liquid bulges suspended at the converged and postprocessed liquid/vapor interfaces supported by the derived fiber bundles,

respectively. The relative tolerances for the derived fiber bundles have been listed in Table 3. Because all the relative tolerances are much less than 1 in Table 3, the sufficient accuracy of the interpolation schemes can be confirmed.

The optimized performance of the derived fiber bundles can be confirmed by comparing them with those derived by setting b_z as 0, where b_z is the nonnegative parameter of the PDE filter in (15) and it is used to control the
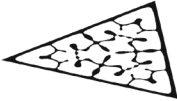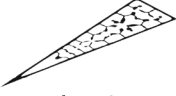
Table 3 Relative tolerances used to evaluate the accuracy of the derived fiber bundles, where the relative tolerance is computed as $|V_c - V_p|/V_p$ with V_c and V_p representing the volumes of the liquid bulges suspended at the liquid/vapor interfaces supported by the converged and postprocessed fiber bundles, respectively

	Fig. 8	Fig. 9	Fig. 10	Fig. 12	Fig. 13	Fig. 14	Fig. 15	Fig. 16
V_c	1.431	3.259	2.340	2.269	2.937	1.152	2.252	3.995
V_p	1.331	2.992	2.165	2.135	2.711	1.060	2.201	3.682
$|V_c - V_p|/V_p$	*0.075*	*0.089*	*0.081*	*0.063*	*0.083*	*0.087*	*0.023*	*0.085*

The relative tolerances have been noted in italic

height of a structural unit. The allowed range for the normalized height of the base structure is $[0, b_z]$. A smaller b_z corresponds to a stronger constraint imposed on the external surface of the base structure. When b_z is set as 0, the approach outlined in Section 2 will completely degenerate into its equivalent counterpart for topology optimization of planar microtextures (Deng et al. 2018). The reference of Deng et al. (2018) has demonstrated the optimality of the planar microtextures derived using the degenerated approach. Therefore, the optimized performance of the derived fiber bundles in Figs. 8, 9, 10, 12, 13, 14, 15, and 16 can be confirmed from their smaller converged values of the performance measurement in Table 4. To further confirm the optimized performance, the fiber bundle derived for the tilling with regular-quadrangle lattices (Fig. 9) is compared with the hierarchical configuration proposed in the reference of Wu et al. (2011) (Fig. 17), where the value of the performance measurement in (12) is improved from 1125 to 9.550 by using topology optimization.

3.2 Effect of duty ratio

For a solid surface with hierarchical microtextures, the duty ratio is a key factor in determining the apparent contact angle, which reflects the macroscale wetting performance of the hierarchical microtextures (Cassie and Baxter 1944). In the hydrophobic case, a smaller duty ratio corresponds to a larger apparent contact angle. Thus, several specified duty ratios in the range from 0.2 to 0.4 have been investigated for the three regular-polygon tilings, with the other parameters chosen to be the same as those in Table 2. By solving the topology optimization problem in (25), the fiber bundles are derived as shown in Fig. 18, which also presents the converged values of the performance measurement. Pareto fronts for the duty ratio in the wider range [0.15, 0.95] have been provided in Fig. 22 for the three regular-polygon tilings in Figs. 8a1, 9a1, and 10a1, respectively. In this wider range, 0, 1, and small values are not included, because 0 and 1 correspond to the structural units without secondary structures and the

Table 4 Converged values of the performance measurement of the fiber bundles derived by setting the height amplitude b_z as 1 and 0, respectively
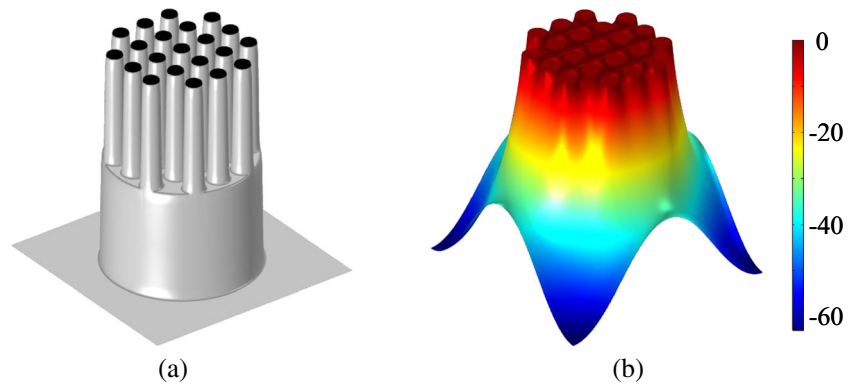

(a) Regular-triangle tiling in Fig. 8		(b) Regular-quadrangle tiling in Fig. 9	
$b_z = 1$	$b_z = 0$	$b_z = 1$	$b_z = 0$
J_c	**3.078**	6.120	J_c	**9.550**	9.937

(c) Regular-hexagon tiling in Fig. 10		(d) Radial tiling in Fig. 12	
$b_z = 1$	$b_z = 0$	$b_z = 1$	$b_z = 0$
J_c	**13.325**	16.269	J_c	**2.126**	6.757

(e) Radial tiling in Fig. 13		(f) Chiral tiling in Fig. 14	
$b_z = 1$	$b_z = 0$	$b_z = 1$	$b_z = 0$
J_c	**0.800**	2.692	J_c	**0.541**	1.808

(g) Chiral tiling in Fig. 15		(h) Penrose tiling in Fig. 16	
$b_z = 1$	$b_z = 0$	$b_z = 1$	$b_z = 0$
J_c	**0.225**	1.136	J_c	**14.412**	49.437

The optimized entries have been noted in bold

(a)   (b)

hierarchy of the microtextures thus degenerates. Also, the liquid/vapor interface supported by the secondary structures has very large deformation and the numerical solution to the Young-Laplace equation is prone to diverge when the duty ratio is very small.

Because a larger duty ratio corresponds to smaller deformation of the liquid/vapor interface, the converged

values of the performance measurement in Fig. 18 approximately decrease with an increase in the duty ratio. This shows that fiber bundles with low duty ratios have relatively weak capability to sustain the liquid/vapor interfaces. This effect decreases as the duty ratio increases. Therefore, a designer can improve the performance of the hierarchical microtextures by setting a reasonably large

Fig. 18 Plots for the converged values of the performance measurement for the fiber bundles derived with different duty ratios, corresponding to the three regular-polygon tilings in Figs. 8a1, 9a1, and 10a1, respectively

(a) Regular triangle

(b) Regular quadrangle

(c) Regular hexagon
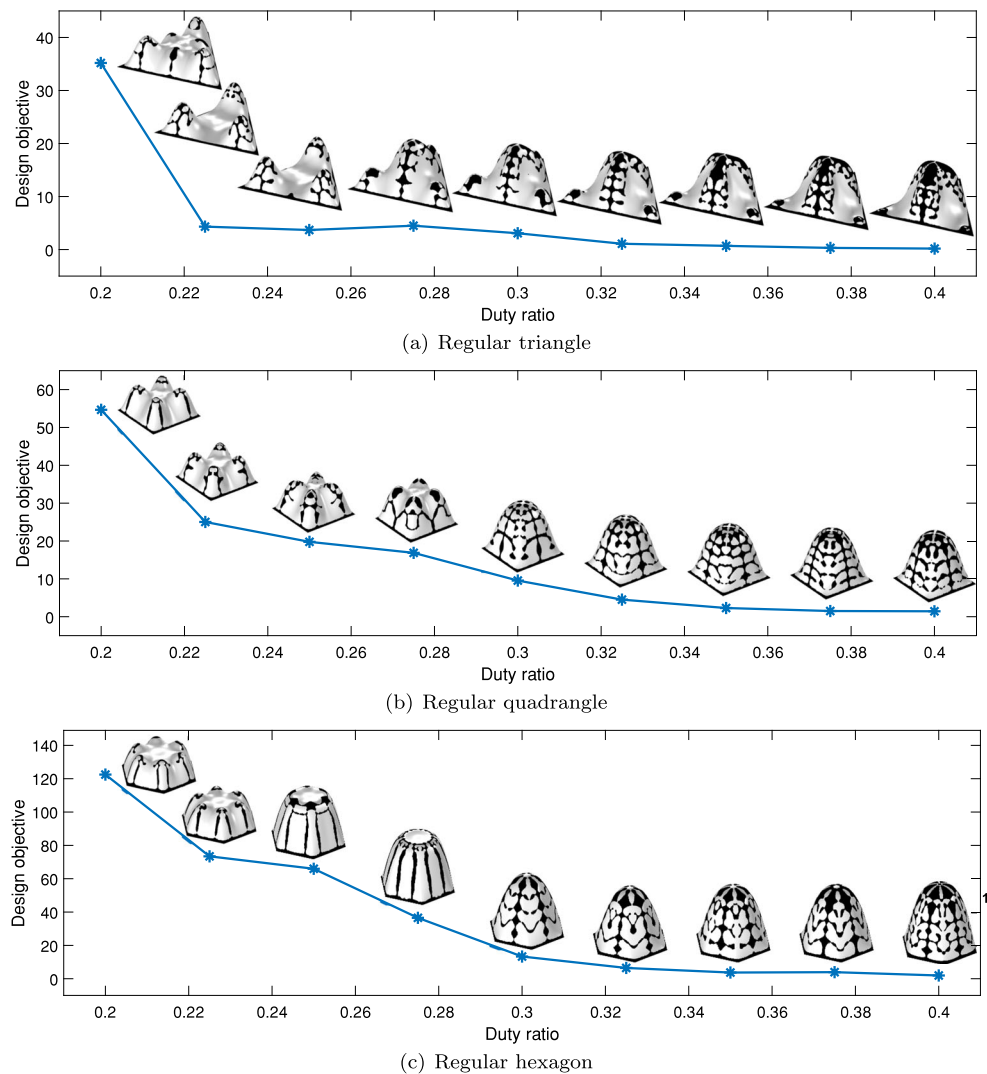
duty ratio because the design objective is to equivalently minimize the volume of the liquid bulges supported at the liquid/vapor interface in the terminal state of the Cassie-Baxter mode.

## 3.3 Volume-fraction constraint for base structure

The fiber bundle for the hierarchical microtextures can be optimized by specifying a volume to be covered by the external surface of the base structure. This can provide an approach to implement the topology optimization of a fiber bundle with a fixed volume of the base structure. The specified volume is derived by adding the following constraint on the volume fraction to the topology optimization problem in (25):

$$|v - v_0| \leq 10^{-3}, \tag{46}$$

where v is the fraction of the volume covered by the external surface of the base structure enclosed by the prism-shaped domain $\Omega \times (0, b_z)$; $v_0 \in (0, v_{0,\sup}]$ is the specified volume fraction, with a permitted tolerance of 10^{-3}; and $v_{0,\sup}$ is the upper bound of v_0, which is the fraction of the volume covered by the surface corresponding to the solution of the

Fig. 19 Plots for the converged values of the performance measurement for the fiber bundles derived by adding constraints on the volume fraction of the base structures, corresponding to the three regular-polygon tilings in Figs. 8a1, 9a1, and 10a1, respectively

(a) Regular triangle

(b) Regular quadrangle

(c) Regular hexagon
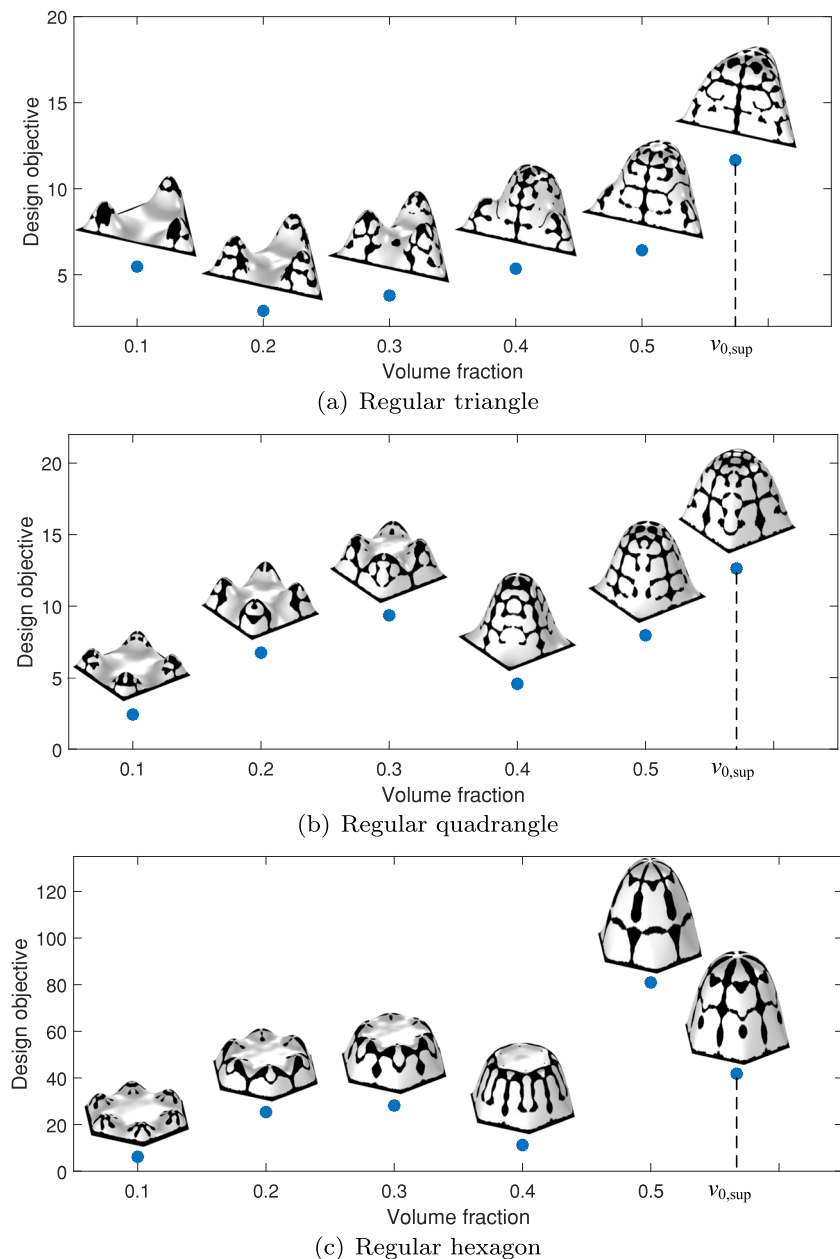
PDE filters in (14) and (15) with the design variable z_m set as 1. The volume fraction v is expressed as

$$v = \frac{1}{b_z |\Omega|} \int_\Omega z_s \, d\Omega, \tag{47}$$

where $|\Omega| = \int_\Omega 1 \, d\Omega$ is the area of Ω.

From the adjoint analysis detailed in Appendix Section 5, the adjoint sensitivity of the volume fraction is derived as

$$\delta v = -\int_\Omega z_{fa} \delta z_m \, d\Omega, \quad \delta z_m \in \mathcal{H}^{-1}(\Omega), \tag{48}$$

where the adjoint variable z_{fa} is derived by sequentially solving the following variational formulations of the adjoint equations:

– Find $z_{sa} \in \mathcal{H}(\Omega)$ with $z_{sa} = 0$ on $\partial\Omega$, satisfying

$$\int_\Omega \frac{1}{b_z |\Omega|} \tilde{z}_{sa} + r_m^2 \nabla z_{sa} \cdot \nabla \tilde{z}_{sa} + z_{sa} \tilde{z}_{sa} \, d\Omega = 0,$$
$$\forall \tilde{z}_{sa} \in \mathcal{H}(\Omega); \tag{49}$$

– Find $z_{fa} \in \mathcal{H}(\Omega)$ with $z_{fa} = 0$ on $\partial\Omega$, satisfying

$$\int_\Omega r_m^2 \nabla z_{fa} \cdot \nabla \tilde{z}_{fa} + z_{fa} \tilde{z}_{fa} - b_z z_{sa} \tilde{z}_{fa} \, d\Omega = 0,$$
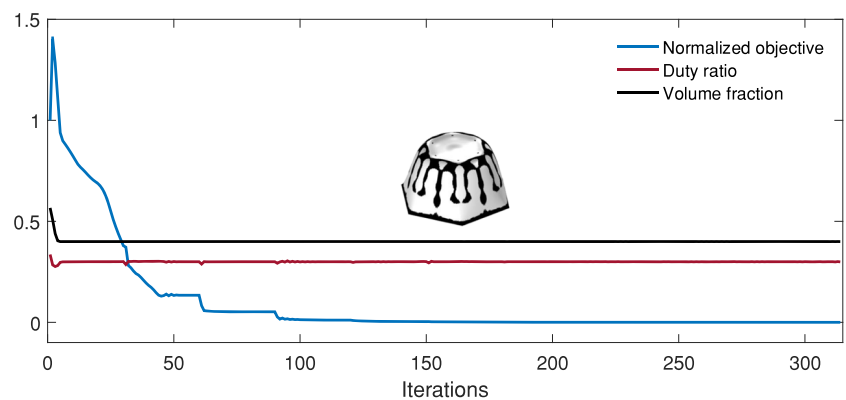$$\forall \tilde{z}_{fa} \in \mathcal{H}(\Omega). \tag{50}$$

Fig. 20 Convergence histories for the derived fiber bundles with the volume fraction specified as 0.4 in the constraint on the volume fraction of the base structure, corresponding to the three regular-polygon tilings in Figs. 8a1, 9a1, and 10a1, respectively
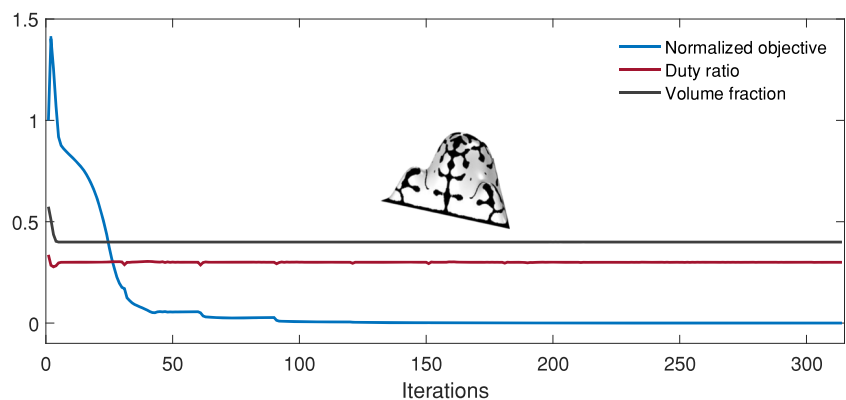
(a) Regular triangle
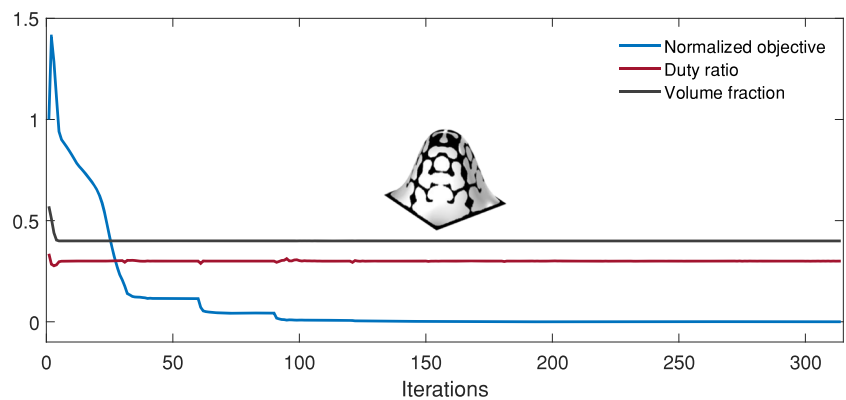
(b) Regular quadrangle

(c) Regular hexagon

By incorporating the constraint on the volume fraction and its adjoint information into the pseudocode in Table 1, fiber bundles for the regular-polygon tilings can be derived by setting the specified volume fractions to be several different values in the feasible set $\left(0, v_{0,\text{sup}}\right]$. The derived results are shown in Fig. 19, together with all the converged values of the design objective, where the upper bound $v_{0,\text{sup}}$ are 0.574, 0.571, and 0.567 for the regular triangular, quadrangular, and hexagonal tilings, respectively. The convergence histories are plotted in Fig. 20 for the cases with the specified volume fraction equal to 0.4. From Fig. 20, we can confirm the volume conservation performance of the constraint on the volume fraction of the base structure and its regularizing effect on the monotonic convergence of the topology optimization procedure.

In Fig. 19, peaks in the base structures are seen to arise at the corners when a relatively small volume fraction is specified; as the specified volume is increased, central peaks tend to arise at the center of the lattice and become thicker, while the corner peaks gradually disappear. Thus, it is demonstrated that the peaks of the base structure can be controlled by imposing a constraint on the volume fraction of the base structure.

3.4 Reduction of model dimension

The dimension of the topology optimization model introduced in Section 2 can be reduced, where the definition domain Ω and the external surface Σ degenerate into a line section on x-axis, and a curved line in the xOz-plane, respectively. The model with reduced dimension corresponds to the one-dimensional (1D) tiling with a strip lattice sketched in Fig. 21a1. The hierarchical microtextures derived by using the model with reduced dimension have extruding configurations with infinite size along the y-axis.

The reduction of the model dimension is implemented by replacing the gradient operator ∇ and the surface gradient operator ∇_s with $(\partial/\partial x)\, \mathbf{i}$ and $(\partial/\partial x)\, \mathbf{i} - \left[(\partial z_s/\partial x)\mathbf{i} - \mathbf{k}\right]/\left(1 + |\partial z_s/\partial x|^2\right)(\partial z_s/\partial x)(\partial/\partial x)$, respectively; and the unitary normal vector of Σ becomes $\mathbf{n}_s = \left[-(\partial z_s/\partial x)\mathbf{i} + \mathbf{k}\right]/\sqrt{1 + |\partial z_s/\partial x|^2}$. Based on this model, a fiber bundle can be derived to efficiently generate the cross-section of the hierarchical microtextures, where the base manifold and the fibers correspond to the cross-sections of the external surface of the base structure, and the pattern of the secondary structures, respectively. With the parameters listed in Table 2, the fiber bundle shown in Fig. 21 is derived for the dimensionless cross-section of

Fig. 21 (a1) Top-view sketch for the one-dimensional tiling of a flat solid surface, where the tiling lattice is a strip with the width of L. (a2) Irreducible line-section domain (gray colored line section) of the cross-section of the dimensionless strip lattice. (b) Perspective view for the cross-section of the external surface of the base structure. (c) Perspective view for the cross-section of the pattern of the secondary structures. (d) Perspective view for the cross-section of the offset fiber bundle. (e) Perspective view in the cross-section for the normalized displacement of the two-phase interfaces relative to the external surface of the base structure
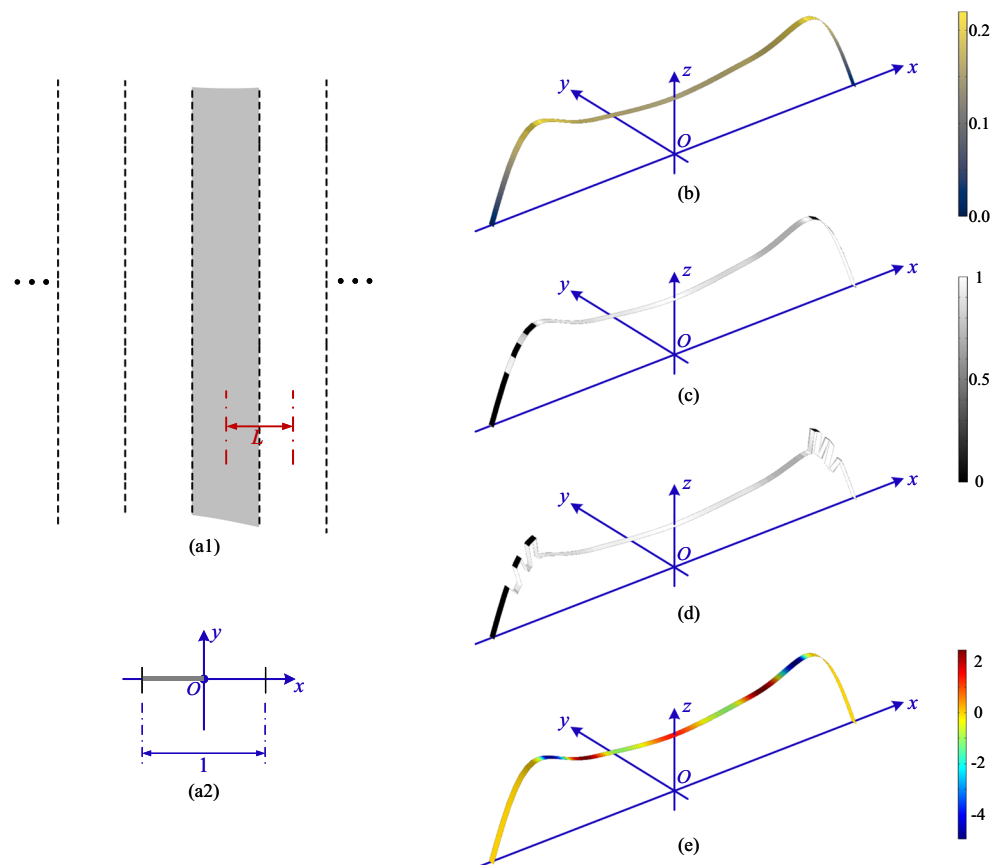
the hierarchical microtextures, where 1D finite elements are used to discretize the dimensionless line-section lattice.

4 Conclusions

This paper has presented the topology optimization of hierarchical microtextures for wetting behaviors in the Cassie-Baxter mode, where the structural configuration is represented in terms of a fiber bundle composed of the base manifold and the fibers corresponding to the external surface of the base structure and the pattern of the secondary structures, respectively. Optimized match between the base manifold and the fibers of the fiber bundle is implemented by solving a topology optimization problem with two design variables. Two sequential PDE filters are applied to the design variable of the base structure, to ensure the curvature smoothness of the external surface of the base structure. These two PDE filters can eliminate the second-order derivative in the term of the base pressure in the Young-Laplace equation, thereby overcoming the difficulties encountered in numerical computation. Because the secondary structures are defined on the implicitly described external surface of the base structure, this topology optimization is implemented on a variable design domain that evolves together with the structure defined on it.

Fiber bundles for the hierarchical microtextures have been derived for the tilings with axial symmetry, radial symmetry, chirality, and quasiperiodicity, respectively. Numerical examples have demonstrated the convergent performance of this presented topology optimization procedure for the hierarchical microtextures. To minimize the volume of the liquid bulges in the terminal state of the Cassie-Baxter mode, fiber bundles are derived with the geometrical configurations consisting of the base structures with the peak shapes and dense secondary structures surrounding the peak crests. The minimization of the volume of the liquid bulges can have the consequences on minimizing the perturbation of the liquid/vapor interface from the base structure and enhancing the pressure resistance of the Cassie-Baxter mode. The hierarchical design with a base structure can help to enhance the stiffness of the microtextures and make them less prone to damage caused by the elastocapillary effect. Imposing a constraint such that the liquid/vapor interface is fixed on the lattice skeletons can create completely enclosed vapor pockets, thus enabling a potential dewetting effect on the derived hierarchical microtextures. Based on the effect of the duty ratio of the fiber bundle, a designer can improve the performance of the hierarchical microtextures

by selecting a reasonable duty ratio. An investigation of the volume fraction of the base structure shows that the peaks of the base structure can be controlled by specifying a reasonable value of this volume fraction. Dimension of the model can be reduced to implement the topology optimization of the cross-sections of the hierarchical microtextures with extruding configurations. In the future, we will explore the micro-/nanofabrication of the derived hierarchical microtextures and experimentally test their wetting performance. This topology optimization procedure can be extended to the optimization of flexible, wearable, and implantable microfluidic devices.

In this paper, the periodicity of the hierarchical microtextures is enforced by a homogeneous boundary condition of the Young-Laplace equation. Although this can offer more symmetry properties beyond axis symmetry of tiling periodicity, the periodicity of some tillings can also be imposed by using the symmetric and periodic boundary conditions, which are less constraining than a homogeneous boundary condition. Moreover, the Cassie-Baxter mode is described by the Young-Laplace equation, in which the liquid/vapor interface is assumed to be a geometrical surface with zero thickness and the dynamic effect of a fluid flow is excluded. However, diffusion intrinsically exits at the liquid/vapor interface. Thus, in reality, the liquid/vapor interface has a thickness at the molecular scale. Therefore, the topology optimization model requires to be updated to also consider molecular misciblity at each liquid/vapor interface with a characteristic size close to the scale of the liquid molecule.

Compliance with Ethical Standards

Conflict of interest The authors declare that they have no conflict of interest.

Replication of results Details on the numerical implementation for the replication of the results have been provided in Section 2.5, with the pseudocode in Table 1 and the optimization parameters in Table 2. The size of the meshes used to discretize the dimensionless design domains in Section 3 has been illustrated in Fig. 7. If the information provided in the paper is not sufficient, we sincerely welcome scientists or interested parties to contact us for further explanations.

Appendix

In Appendixes 1–5, the variational formulations of the related PDEs and the adjoint equations are detailed, based on the Kurash-Kuhn-Tucker (KKT) condition of the PDE constrained optimization problem and Lagrangian multiplier-based adjoint method (Hinze et al. 2009). In Appendix 1, Pareto fronts for the duty ratio of the fiber bundles for the hierarchical microtextures are provided.

Appendix 1: Variational formulations of PDEs

Based on the Galerkin variational principle, the variational formulations of the related PDEs can be derived as

– Variational formulation of the PDE filter in (14):
find $z_f \in \mathcal{H}(\Omega)$ with $z_f = 0$ on $\partial\Omega$, satisfying

$$\int_\Omega r_m^2 \nabla z_f \cdot \nabla \tilde{z}_f + z_f \tilde{z}_f - z_m \tilde{z}_f \, \mathrm{d}\Omega = 0,$$
$$\forall \tilde{z}_f \in \mathcal{H}(\Omega); \tag{51}$$

– Variational formulation of the PDE filter in (15):
find $z_s \in \mathcal{H}(\Omega)$ with $z_s = 0$ on $\partial\Omega$, satisfying

$$\int_\Omega r_m^2 \nabla z_s \cdot \nabla \tilde{z}_s + z_s \tilde{z}_s - b_z z_f \tilde{z}_s \, \mathrm{d}\Omega = 0,$$
$$\forall \tilde{z}_s \in \mathcal{H}(\Omega); \tag{52}$$

– Variational formulation of the surface-PDE filter in (17):
find $\gamma_f \in \mathcal{H}(\Sigma)$ with $\gamma_f = 0$ at $\partial\Sigma$, satisfying

$$\int_\Sigma r_f^2 \nabla_s \gamma_f \cdot \nabla_s \tilde{\gamma}_f + \gamma_f \tilde{\gamma}_f - \gamma \tilde{\gamma}_f \, \mathrm{d}\Sigma = 0,$$
$$\forall \tilde{\gamma}_f \in \mathcal{H}(\Sigma); \tag{53}$$

– Variational formulation of the dimensionless Young-Laplace (24):
find $\bar{d} \in \mathcal{H}(\Sigma)$ with $\bar{d} = 0$ at $\partial\Sigma$ and $\kappa \in \mathcal{H}^{-1}(\Omega)$, satisfying

$$\int_\Sigma -\bar{\sigma} \frac{\nabla_s \bar{d} \cdot \nabla_s \tilde{\bar{d}}}{\sqrt{1/d_0^2 + |\nabla_s \bar{d}|^2}} - (1 - p_\kappa \kappa) \tilde{\bar{d}} \, \mathrm{d}\Sigma$$
$$+ \int_\Omega \left[\kappa - \frac{\bar{\sigma}_l}{r_m^2} \frac{z_s - b_z z_f}{\left(\sqrt{1 + |\nabla z_s|^2}\right)^3} \right] \tilde{\kappa} \, \mathrm{d}\Omega = 0,$$
$$\forall \tilde{\bar{d}} \in \mathcal{H}(\Sigma) \text{ and } \forall \tilde{\kappa} \in \mathring{\mathcal{H}}(\Omega) \tag{54}$$

where $\tilde{z}_f$, $\tilde{z}_s$, $\tilde{\gamma}_f$, $\tilde{\bar{d}}$, and $\tilde{\kappa}$ are the test functions of z_f, z_s, γ_f, $\bar{d}$, and κ, respectively; $\mathcal{H}(\Sigma)$ and $\mathcal{H}(\Omega)$ are the first order Sobolev spaces on Σ and Ω, respectively; $\mathring{\mathcal{H}}(\Omega)$ is the closure of $C_0^\infty(\Omega)$; $\mathcal{H}^{-1}(\Omega)$ is the dual space of $\mathring{\mathcal{H}}(\Omega)$.

Appendix 2: Adjoint analysis for $J|\Sigma|^2$ in design objective

Based on the variational formulations of the PDEs in (51–54) and Lagrangian multiplier-based adjoint method, the augmented Lagrangian for $J|\Sigma|^2 = \int_\Sigma \bar{d}^2 \, \mathrm{d}\Sigma$ can be formulated as

$$\widehat{J|\Sigma|^2} = \int_\Sigma \bar{d}^2 - \bar{\sigma} \frac{\nabla_s \bar{d} \cdot \nabla_s \bar{d}_a}{\sqrt{1/d_0^2 + |\nabla_s \bar{d}|^2}} - (1 - p_\kappa \kappa) \bar{d}_a$$
$$+ r_f^2 \nabla_s \gamma_f \cdot \nabla_s \gamma_{fa} + \gamma_f \gamma_{fa} - \gamma \gamma_{fa} \, \mathrm{d}\Sigma$$
$$+ \int_\Omega \left[\kappa - \frac{\bar{\sigma}_l}{r_m^2} \frac{z_s - b_z z_f}{\left(\sqrt{1 + |\nabla z_s|^2}\right)^3} \right] \kappa_a + r_m^2 \nabla z_f$$
$$\cdot \nabla z_{fa} + z_f z_{fa} - z_m z_{fa} + r_m^2 \nabla z_s \cdot \nabla z_{sa}$$
$$+ z_s z_{sa} - b_z z_f z_{sa} \, \mathrm{d}\Omega$$
$$= \int_\Omega \left[\bar{d}^2 - \bar{\sigma} \frac{\nabla_s \bar{d} \cdot \nabla_s \bar{d}_a}{\sqrt{1/d_0^2 + |\nabla_s \bar{d}|^2}} - (1 - p_\kappa \kappa) \bar{d}_a \right.$$
$$\left. + r_f^2 \nabla_s \gamma_f \cdot \nabla_s \gamma_{fa} + \gamma_f \gamma_{fa} - \gamma \gamma_{fa} \right]$$
$$\times \sqrt{1 + |\nabla z_s|^2} + \left[\kappa - \frac{\bar{\sigma}_l}{r_m^2} \frac{z_s - b_z z_f}{\left(\sqrt{1 + |\nabla z_s|^2}\right)^3} \right]$$
$$\times \kappa_a + r_m^2 \nabla z_f \cdot \nabla z_{fa} + z_f z_{fa} - z_m z_{fa}$$
$$+ r_m^2 \nabla z_s \cdot \nabla z_{sa} + z_s z_{sa} - b_z z_f z_{sa} \, \mathrm{d}\Omega, \tag{55}$$

where $\bar{d}_a = 0$ and $\gamma_{fa} = 0$ are satisfied at $\partial\Sigma$; $z_{fa} = 0$ and $z_{sa} = 0$ are satisfied on $\partial\Omega$. The first-order variational of the augmented Lagrangian $\hat{J}$ is

$$\widehat{\delta J |\Sigma|^2} = \int_\Omega \left[2\bar{d}\delta\bar{d} - \bar{\sigma}\frac{\nabla_s\delta\bar{d}\cdot\nabla_s\bar{d}_a}{\sqrt{1/d_0^2 + |\nabla_s\bar{d}|^2}} + \bar{\sigma}\frac{(\nabla_s\bar{d}\cdot\nabla_s\bar{d}_a)(\nabla_s\bar{d}\cdot\nabla_s\delta\bar{d})}{\left(\sqrt{1/d_0^2 + |\nabla_s\bar{d}|^2}\right)^3} \right]\sqrt{1 + |\nabla z_s|^2} + p_\kappa\bar{d}_a\sqrt{1 + |\nabla z_s|^2}\delta\kappa$$

$$+ \kappa_a\delta\kappa + \left(r_f^2\nabla_s\delta\gamma_f\cdot\nabla_s\gamma_{fa} + \delta\gamma_f\gamma_{fa} - \frac{\partial\bar{\sigma}}{\partial\gamma_p}\frac{\partial\gamma_p}{\partial\gamma_f}\frac{\nabla_s\bar{d}\cdot\nabla_s\bar{d}_a}{\sqrt{1/d_0^2 + |\nabla_s\bar{d}|^2}}\delta\gamma_f + \frac{\partial p_\kappa}{\partial\gamma_p}\frac{\partial\gamma_p}{\partial\gamma_f}\kappa\bar{d}_a\delta\gamma_f \right)\sqrt{1 + |\nabla z_s|^2}$$

$$- \gamma_{fa}\sqrt{1 + |\nabla z_s|^2}\delta\gamma + r_m^2\nabla\delta z_f\cdot\nabla z_{fa} + \delta z_f z_{fa} + r_m^2\nabla\delta z_s\cdot\nabla z_{sa} + \delta z_s z_{sa} - b_z\delta z_f z_{sa}$$

$$+ r_f^2\left[\nabla_s^{(\delta z_s)}\gamma_f\cdot\nabla_s\gamma_{fa} + \nabla_s\gamma_f\cdot\nabla_s^{(\delta z_s)}\gamma_{fa}\right]\sqrt{1 + |\nabla z_s|^2}$$

$$- \bar{\sigma}\left[\frac{\nabla_s^{(\delta z_s)}\bar{d}\cdot\nabla_s\bar{d}_a + \nabla_s\bar{d}\cdot\nabla_s^{(\delta z_s)}\bar{d}_a}{\sqrt{1/d_0^2 + |\nabla_s\bar{d}|^2}} - \frac{(\nabla_s\bar{d}\cdot\nabla_s\bar{d}_a)(\nabla_s^{(\delta z_s)}\bar{d}\cdot\nabla_s\bar{d})}{\left(\sqrt{1/d_0^2 + |\nabla_s\bar{d}|^2}\right)^3}\right]\sqrt{1 + |\nabla z_s|^2}$$

$$+ \left[\bar{d}^2 - \bar{\sigma}\frac{\nabla_s\bar{d}\cdot\nabla_s\bar{d}_a}{\sqrt{1/d_0^2 + |\nabla_s\bar{d}|^2}} - (1 - p_\kappa\kappa)\bar{d}_a + r_f^2\nabla_s\gamma_f\cdot\nabla_s\gamma_{fa} + \gamma_f\gamma_{fa} - \gamma\gamma_{fa}\right]\frac{\nabla z_s\cdot\nabla\delta z_s}{\sqrt{1 + |\nabla z_s|^2}}$$

$$- \frac{\bar{\sigma}_l}{r_m^2}\left[\frac{\delta z_s - b_z\delta z_f}{\left(\sqrt{1 + |\nabla z_s|^2}\right)^3} - 3\frac{(z_s - b_z z_f)(\nabla z_s\cdot\nabla\delta z_s)}{\left(\sqrt{1 + |\nabla z_s|^2}\right)^5}\right]\kappa_a - z_{fa}\delta z_m \, d\Omega, \tag{56}$$

where ∇_s has the transformed form in (19), and its first order variational to z_s has the form as that in (21) with $\tilde{z}_s$ replaced to be δz_s; δz_s, δz_f, δz_m, $\delta\gamma_f$, and $\delta\gamma$ are the first-order variational of z_s, z_f, z_m, γ_f, and γ, respectively. According to the KKT condition of the PDE constrained optimization problem (Hinze et al. 2009), the first-order variational of the augmented Lagrangian to the variables $\bar{d}$, $\bar{\gamma}_f$, z_f, and z_s can be set to be zero as follows:

$$\int_\Omega \left[2\bar{d}\delta\bar{d} - \bar{\sigma}\frac{\nabla_s\bar{d}_a\cdot\nabla_s\delta\bar{d}}{\sqrt{1/d_0^2 + |\nabla_s\bar{d}|^2}} + \bar{\sigma}\frac{(\nabla_s\bar{d}\cdot\nabla_s\bar{d}_a)(\nabla_s\bar{d}\cdot\nabla_s\delta\bar{d})}{\left(\sqrt{1/d_0^2 + |\nabla_s\bar{d}|^2}\right)^3} \right]\sqrt{1 + |\nabla z_s|^2} \, d\Omega = 0$$

$$\Rightarrow \int_\Sigma 2\bar{d}\delta\bar{d} - \bar{\sigma}\frac{\nabla_s\bar{d}_a\cdot\nabla_s\delta\bar{d}}{\sqrt{1/d_0^2 + |\nabla_s\bar{d}|^2}} + \bar{\sigma}\frac{(\nabla_s\bar{d}\cdot\nabla_s\bar{d}_a)(\nabla_s\bar{d}\cdot\nabla_s\delta\bar{d})}{\left(\sqrt{1/d_0^2 + |\nabla_s\bar{d}|^2}\right)^3} \, d\Sigma = 0; \tag{57}$$

$$\int_\Omega \left(p_\kappa\bar{d}_a\sqrt{1 + |\nabla z_s|^2} + \kappa_a \right)\delta\kappa \, d\Omega = 0; \tag{58}$$

$$\int_\Omega \left(r_f^2 \nabla_s \delta\gamma_f \cdot \nabla_s \gamma_{fa} + \delta\gamma_f \gamma_{fa} - \frac{\partial\bar\sigma}{\partial\gamma_p}\frac{\partial\gamma_p}{\partial\gamma_f}\frac{\nabla_s\bar{d}\cdot\nabla_s\bar{d}_a}{\sqrt{1/d_0^2+|\nabla_s\bar{d}|^2}}\delta\gamma_f + \frac{\partial p_\kappa}{\partial\gamma_p}\frac{\partial\gamma_p}{\partial\gamma_f}\kappa\bar{d}_a\delta\gamma_f \right) \sqrt{1+|\nabla z_s|^2}\,\mathrm{d}\Omega = 0$$

$$\Rightarrow \int_\Sigma r_f^2 \nabla_s \delta\gamma_f \cdot \nabla_s \gamma_{fa} + \delta\gamma_f \gamma_{fa} - \frac{\partial\bar\sigma}{\partial\gamma_p}\frac{\partial\gamma_p}{\partial\gamma_f}\frac{\nabla_s\bar{d}\cdot\nabla_s\bar{d}_a}{\sqrt{1/d_0^2+|\nabla_s\bar{d}|^2}}\delta\gamma_f + \frac{\partial p_\kappa}{\partial\gamma_p}\frac{\partial\gamma_p}{\partial\gamma_f}\kappa\bar{d}_a\delta\gamma_f \,\mathrm{d}\Sigma = 0; \tag{59}$$

$$\int_\Omega r_m^2 \nabla\delta z_s \cdot \nabla z_{sa} + \delta z_s z_{sa} + r_f^2\left(\nabla_s^{(\delta z_s)}\gamma_f \cdot \nabla_s\gamma_{fa} + \nabla_s\gamma_f \cdot \nabla_s^{(\delta z_s)}\gamma_{fa}\right)\sqrt{1+|\nabla z_s|^2}$$

$$-\bar\sigma\left[\frac{\nabla_s^{(\delta z_s)}\bar{d}\cdot\nabla_s\bar{d}_a + \nabla_s\bar{d}\cdot\nabla_s^{(\delta z_s)}\bar{d}_a}{\sqrt{1/d_0^2+|\nabla_s\bar{d}|^2}} - \frac{\left(\nabla_s\bar{d}\cdot\nabla_s\bar{d}_a\right)\left(\nabla_s^{(\delta z_s)}\bar{d}\cdot\nabla_s\bar{d}\right)}{\left(\sqrt{1/d_0^2+|\nabla_s\bar{d}|^2}\right)^3}\right]\sqrt{1+|\nabla z_s|^2}$$

$$+\left[\bar{d}^2 - \bar\sigma\frac{\nabla_s\bar{d}\cdot\nabla_s\bar{d}_a}{\sqrt{1/d_0^2+|\nabla_s\bar{d}|^2}} - (1-p_\kappa\kappa)\bar{d}_a + r_f^2\nabla_s\gamma_f\cdot\nabla_s\gamma_{fa} + \gamma_f\gamma_{fa} - \gamma\gamma_{fa}\right]\frac{\nabla z_s\cdot\nabla\delta z_s}{\sqrt{1+|\nabla z_s|^2}}$$

$$-\frac{\bar\sigma_l}{r_m^2}\left[\frac{\delta z_s}{\left(\sqrt{1+|\nabla z_s|^2}\right)^3} - 3\frac{(z_s-b_z z_f)(\nabla z_s\cdot\nabla\delta z_s)}{\left(\sqrt{1+|\nabla z_s|^2}\right)^5}\right]\kappa_a\,\mathrm{d}\Omega = 0; \tag{60}$$

$$\int_\Omega r_m^2\nabla\delta z_f\cdot\nabla z_{fa} + \delta z_f z_{fa} - b_z\delta z_f z_{sa}$$

$$+\frac{\bar\sigma_l}{r_m^2}\frac{b_z\kappa_a}{\left(\sqrt{1+|\nabla z_s|^2}\right)^3}\delta z_f\,\mathrm{d}\Omega = 0. \tag{61}$$

Further, the adjoint sensitivity of $J\,|\Sigma|^2$ is derived from $\widehat{\delta J\,|\Sigma|^2}$:

$$\delta\left(J\,|\Sigma|^2\right) = -\int_\Omega \gamma_{fa}\sqrt{1+|\nabla z_s|^2}\delta\gamma + z_{fa}\delta z_m\,\mathrm{d}\Omega$$

$$= -\int_\Sigma \gamma_{fa}\delta\gamma\,\mathrm{d}\Sigma - \int_\Omega z_{fa}\delta z_m\,\mathrm{d}\Omega. \tag{62}$$

Without losing the arbitrariness of $\delta\bar{d}$, $\delta\kappa$, $\delta\gamma_f$, δz_f, and δz_s, one can set $\delta\bar{d} = \tilde{\bar{d}}_a$ with $\forall\tilde{\bar{d}}_a \in \mathcal{H}(\Sigma)$, $\delta\kappa = \tilde\kappa_a$ with $\forall\tilde\kappa_a \in \mathcal{H}^{-1}(\Omega)$, $\delta\gamma_f = \tilde\gamma_{fa}$ with $\forall\tilde\gamma_{fa} \in \mathcal{H}(\Sigma)$, $\delta z_f = \tilde z_{fa}$ with $\forall\tilde z_{fa} \in \mathcal{H}(\Omega)$, and $\delta z_s = \tilde z_{sa}$ with $\forall\tilde z_{sa} \in \mathcal{H}(\Omega)$, to derive the variational formulations of the adjoint system in (29–32).

Appendix 3: Adjoint analysis for manifold area $|\Sigma|$ in design objective and duty-ratio constraint

Based on the variational formulations of the PDEs in (51) and (52) and the Lagrangian multiplier-based adjoint method, the augmented Lagrangian for $|\Sigma| = \int_\Sigma 1\,\mathrm{d}\Sigma = \int_\Omega \sqrt{1+|\nabla z_s|^2}\,\mathrm{d}\Omega$ can be formulated as

$$\widehat{|\Sigma|} = \int_\Sigma 1\,\mathrm{d}\Sigma + \int_\Omega r_m^2\nabla z_f\cdot\nabla z_{fa} + z_f z_{fa} - z_m z_{fa}$$

$$+r_m^2\nabla z_s\cdot\nabla z_{sa} + z_s z_{sa} - b_z z_f z_{sa}\,\mathrm{d}\Omega$$

$$= \int_\Omega \sqrt{1+|\nabla z_s|^2} + r_m^2\nabla z_f\cdot\nabla z_{fa} + z_f z_{fa} - z_m z_{fa}$$

$$+r_m^2\nabla z_s\cdot\nabla z_{sa} + z_s z_{sa} - b_z z_f z_{sa}\,\mathrm{d}\Omega, \tag{63}$$

where $z_{fa} = 0$ and $z_{sa} = 0$ are satisfied on $\partial\Omega$. The first-order variational of the augmented Lagrangian $\widehat{|\Sigma|}$ is

$$\delta\widehat{|\Sigma|} = \int_\Omega \frac{\nabla z_f\cdot\nabla\delta z_f}{\sqrt{1+|\nabla z_f|^2}} + r_m^2\nabla\delta z_f\cdot\nabla z_{fa} + \delta z_f z_{fa}$$

$$-\delta z_m z_{fa} + r_m^2\nabla\delta z_s\cdot\nabla z_{sa} + \delta z_s z_{sa} - b_z\delta z_f z_{sa}\,\mathrm{d}\Omega. \tag{64}$$

According to the KKT condition of the PDE constrained optimization problem, the first-order variational of the augmented Lagrangian to the variables z_f and z can be set to be zero:

$$\int_\Omega \frac{\nabla z_s\cdot\nabla\delta z_s}{\sqrt{1+|\nabla z_s|^2}} + r_m^2\nabla\delta z_s\cdot\nabla z_{sa} + \delta z_s z_{sa}\,\mathrm{d}\Omega = 0; \tag{65}$$

$$\int_\Omega r_m^2 \nabla \delta z_f \cdot \nabla z_{fa} + \delta z_f z_{fa} - b_z z_{sa} \delta z_f \, d\Omega = 0. \quad (66)$$

Further, the adjoint sensitivity of $|\Sigma|$ is derived from $\delta \widehat{|\Sigma|}$:

$$\delta \, |\Sigma| = -\int_\Omega z_{fa} \delta z_m \, d\Omega. \quad (67)$$

Without losing the arbitrariness of δz_s and δz_f, one can set $\delta z_s = \tilde{z}_{sa}$ with $\forall \tilde{z}_{sa} \in \mathcal{H}(\Omega)$ and $\delta z_f = \tilde{z}_{fa}$ with $\forall \tilde{z}_{fa} \in \mathcal{H}(\Omega)$, to derive the variational formulations of the adjoint system in (35) and (36).

Appendix 4: Adjoint analysis for $f_d \, |\Sigma|$ in duty-ratio constraint

Based on the variational formulations of the PDEs in (51–53) and Lagrangian multiplier-based adjoint method, the augmented Lagrangian for $f_d \, |\Sigma| = \int_\Sigma 1 - \gamma_p \, d\Sigma$ can be formulated as

$$\widehat{f_d \, |\Sigma|} = \int_\Sigma 1 - \gamma_p + r_f^2 \nabla_s \gamma_f \cdot \nabla_s \gamma_{fa} + \gamma_f \gamma_{fa} - \gamma \gamma_{fa} \, d\Sigma$$
$$+ \int_\Omega r_m^2 \nabla z_f \cdot \nabla z_{fa} + z_f z_{fa} - z_m z_{fa} \, d\Omega$$
$$+ \int_\Omega r_m^2 \nabla z_s \cdot \nabla z_{sa} + z_s z_{sa} - b_z z_f z_{sa} \, d\Omega$$
$$= \int_\Omega \left(1 - \gamma_p + r_f^2 \nabla_s \gamma_f \cdot \nabla_s \gamma_{fa} + \gamma_f \gamma_{fa} - \gamma \gamma_{fa}\right)$$
$$\times \sqrt{1 + |\nabla z_s|^2} + r_m^2 \nabla z_f \cdot \nabla z_{fa} + z_f z_{fa} - z_m z_{fa}$$
$$+ r_m^2 \nabla z_s \cdot \nabla z_{sa} + z_s z_{sa} - b_z z_f z_{sa} \, d\Omega, \quad (68)$$

where $\gamma_{fa} = 0$ is satisfied at $\partial \Sigma$; $z_{fa} = 0$ is satisfied on $\partial \Omega$. The first-order variational of the augmented Lagrangian $\widehat{f_d \, |\Sigma|}$ is

$$\delta \widehat{f_d \, |\Sigma|} = \int_\Omega \left(-\frac{\partial \gamma_p}{\partial \gamma_f} \delta \gamma_f + r_f^2 \nabla_s \delta \gamma_f \cdot \nabla_s \gamma_{fa} + \delta \gamma_f \gamma_{fa}\right.$$
$$\left. - \delta \gamma \gamma_{fa}\right) \sqrt{1 + |\nabla z_s|^2}$$
$$+ r_f^2 \left(\nabla_s^{(\delta z_s)} \gamma_f \cdot \nabla_s \gamma_{fa} + \nabla_s \gamma_f \cdot \nabla_s^{(\delta z_s)} \gamma_{fa}\right)$$
$$\times \sqrt{1 + |\nabla z_s|^2}$$
$$+ \left(1 - \gamma_p + r_f^2 \nabla_s \gamma_f \cdot \nabla_s \gamma_{fa} + \gamma_f \gamma_{fa} - \gamma \gamma_{fa}\right)$$
$$\times \frac{\nabla z_s \cdot \nabla \delta z_s}{\sqrt{1 + |\nabla z_s|^2}} + r_m^2 \nabla \delta z_f \cdot \nabla z_{fa} + \delta z_f z_{fa}$$
$$- \delta z_m z_{fa} + r_m^2 \nabla \delta z_s \cdot \nabla z_{sa} + \delta z_s z_{sa}$$
$$- b_z \delta z_f z_{sa} \, d\Omega. \quad (69)$$

According to the KKT condition of the PDE constrained optimization problem, the first-order variational of the

augmented Lagrangian to the variables γ_f, z_f, and z_s can be set to be zero:

$$\int_\Omega \left(-\frac{\partial \gamma_p}{\partial \gamma_f} \delta \gamma_f + r_f^2 \nabla_s \delta \gamma_f \cdot \nabla_s \gamma_{fa} + \delta \gamma_f \gamma_{fa}\right)$$
$$\times \sqrt{1 + |\nabla z_s|^2} \, d\Omega = 0$$
$$\Rightarrow \int_\Sigma -\frac{\partial \gamma_p}{\partial \gamma_f} \delta \gamma_f + r_f^2 \nabla_s \delta \gamma_f \cdot \nabla_s \gamma_{fa} + \delta \gamma_f \gamma_{fa} \, d\Sigma = 0; \quad (70)$$

$$\int_\Omega r_f^2 \left(\nabla_s^{(\delta z_s)} \gamma_f \cdot \nabla_s \gamma_{fa} + \nabla_s \gamma_f \cdot \nabla_s^{(\delta z_s)} \gamma_{fa}\right) \sqrt{1 + |\nabla z_s|^2}$$
$$+ \left(1 - \gamma_p + r_f^2 \nabla_s \gamma_f \cdot \nabla_s \gamma_{fa} + \gamma_f \gamma_{fa} - \gamma \gamma_{fa}\right)$$
$$\times \frac{\nabla z_s \cdot \nabla \delta z_s}{\sqrt{1 + |\nabla z_s|^2}} + r_m^2 \nabla \delta z_s \cdot \nabla z_{sa} + \delta z_s z_{sa} \, d\Omega = 0; \quad (71)$$

$$\int_\Omega r_m^2 \nabla \delta z_f \cdot \nabla z_{fa} + \delta z_f z_{fa} - b_z z_{sa} \delta z_f \, d\Omega = 0. \quad (72)$$

Further, the adjoint sensitivity of $f_d \, |\Sigma|$ is derived from $\delta \widehat{f_d \, |\Sigma|}$:

$$\delta (f_d \, |\Sigma|) = -\int_\Omega \gamma_{fa} \sqrt{1 + |\nabla z_s|^2} \delta \gamma + z_{fa} \delta z_m \, d\Omega$$
$$= -\int_\Sigma \gamma_{fa} \delta \gamma \, d\Sigma - \int_\Omega z_{fa} \delta z_m \, d\Omega. \quad (73)$$

Without losing the arbitrariness of $\delta \gamma_f$, δz_f, and δz_s, one can set $\delta \gamma_f = \tilde{\gamma}_{fa}$ with $\forall \tilde{\gamma}_{fa} \in \mathcal{H}(\Sigma)$, $\delta z_f = \tilde{z}_{fa}$ with $\forall \tilde{z}_{fa} \in \mathcal{H}(\Omega)$, and $\delta z_s = \tilde{z}_{sa}$ with $\forall \tilde{z}_{sa} \in \mathcal{H}(\Omega)$, to derive the variational formulations of the adjoint system in (39) and (40).

Appendix 5: Adjoint analysis for v in volume-fraction constraint

Based on the variational formulations of the PDEs in (51) and (52) and the Lagrangian multiplier-based adjoint method, the augmented Lagrangian for $v = \int_\Omega z_s \, d\Sigma / (b_z \, |\Omega|)$ can be formulated as
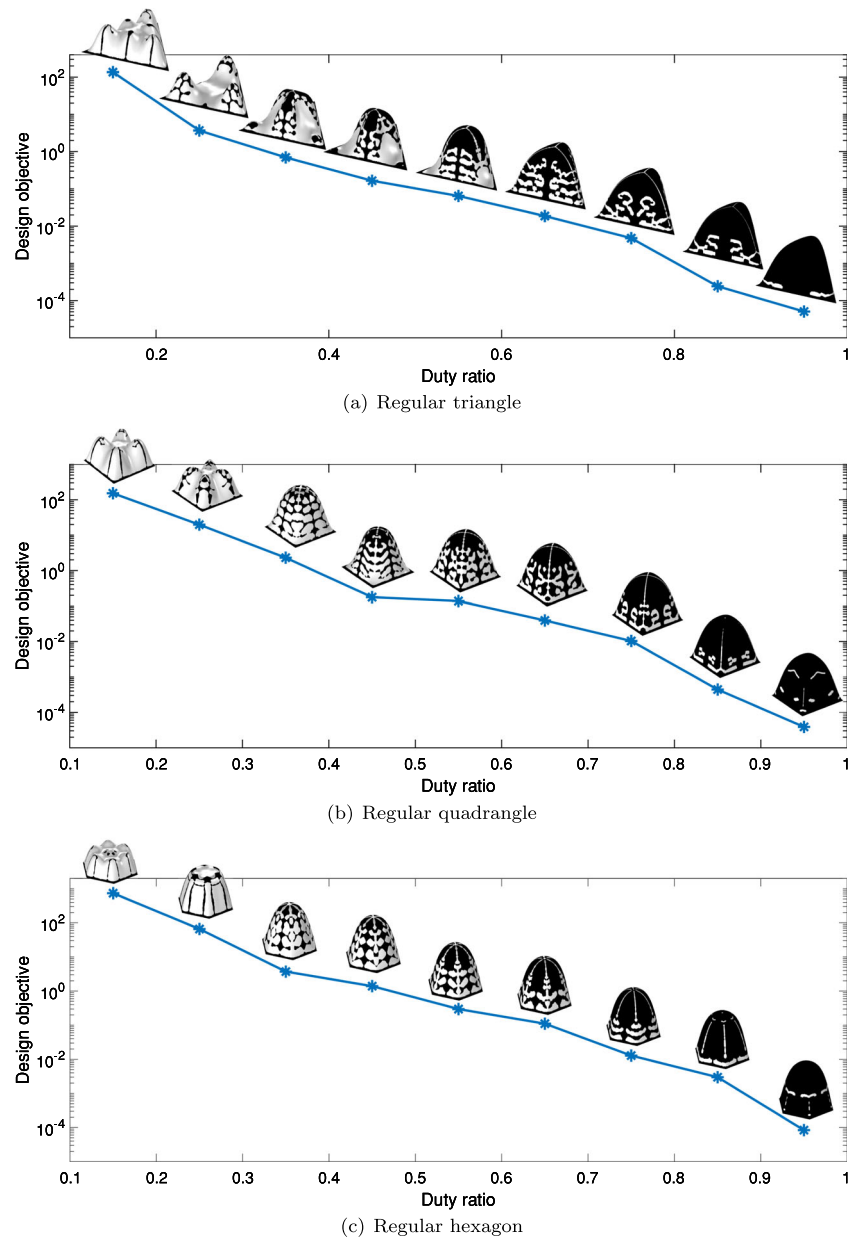
$$\hat{v} = \int_\Omega \frac{1}{b_z \, |\Omega|} z_s + r_m^2 \nabla z_f \cdot \nabla z_{fa} + z_f z_{fa} - z_m z_{fa}$$
$$+ r_m^2 \nabla z_s \cdot \nabla z_{sa} + z_s z_{sa} - b_z z_f z_{sa} \, d\Omega. \quad (74)$$

where $z_{fa} = 0$ is satisfied on $\partial \Omega$. The first-order variational of the augmented Lagrangian $\hat{v}$ is

$$\delta \hat{v} = \int_\Omega \frac{1}{b_z \, |\Omega|} \delta z_s + r_m^2 \nabla \delta z_f \cdot \nabla z_{fa} + \delta z_f z_{fa} - \delta z_m z_{fa}$$
$$+ r_m^2 \nabla \delta z_s \cdot \nabla z_{sa} + \delta z_s z_{sa} - b_z \delta z_f z_{sa} \, d\Omega. \quad (75)$$

According to the KKT condition of the PDE constrained optimization problem, the first-order variational of the

Fig. 22 Plots for the converged values of the performance measurement for the derived fiber bundles with different duty ratios, corresponding to the three regular-polygon tilings in Figs. 8a1, 9a1 and 10a1, respectively

(a) Regular triangle

(b) Regular quadrangle

(c) Regular hexagon

augmented Lagrangian to the variable z_s and z_f can be set to be zero:

$$\int_\Omega \frac{1}{b_z |\Omega|} \delta z_s + r_m^2 \nabla \delta z_s \cdot \nabla z_{sa} + \delta z_s z_{sa} \, \mathrm{d}\Omega = 0; \qquad (76)$$

$$\int_\Omega r_m^2 \nabla \delta z_f \cdot \nabla z_{fa} + \delta z_f z_{fa} - b_z \delta z_f z_{sa} \, \mathrm{d}\Omega = 0. \qquad (77)$$

Further, the adjoint sensitivity of v is derived from $\delta \hat{v}$:

$$\delta v = -\int_\Omega z_{fa} \delta z_m \, \mathrm{d}\Omega. \qquad (78)$$

Without losing the arbitrariness of δz_s and δz_f, one can set $\delta z_s = \tilde{z}_{sa}$ with $\forall \tilde{z}_{sa} \in \mathcal{H}(\Omega)$ and $\delta z_f = \tilde{z}_{fa}$ with

$\forall \tilde{z}_{fa} \in \mathcal{H}(\Omega)$, to derive the variational formulations of the adjoint system in (49) and (50).

References

Allaire G, Dapogny C, Delgado G, Michailidis G (2014) Multi-phase structural optimization via a level set method. ESAIM: Control Optim Calc Var 20:576–611

Andreasen CS, Sigmund O (2012) Multiscale modeling and topology optimization of poroelastic actuators. Smart Mater Struct 21:065005

Andreasen CS (2020) A framework for topology optimization of inertial microfluidic particle manipulators. Struct Multidisc Optim. https://doi.org/10.1007/s00158-019-02483-5

Ansola R, Canales J, Tárrago JA, Rasmussen J (2002) An integrated approach for shape and topology optimization of shell structures. Comput Struct 80:449–458

Aulig N, Lepenies I (2012) A topology optimization interface for LS-DYNA. In: 11. LS-DYNA Forum, ulm

Behrou R, Lawry M, Maute K (2017) Level set topology optimization of structural problems with interface cohesion. Int J Numer Meth Eng 112:990–1016

Bendsøe MP, Kikuchi N (1988) Generating optimal topologies in optimal design using a homogenization method. Comput Methods Appl Mech Eng 71:197–224

Bendsøe MP (1995) Optimization of structural topology, shape and material. Springer, Berlin

Bendsøe MP, Sigmund O (1999) Material interpolations in topology optimization. Arch Appl Mech 69:635–654

Bendsøe MP, Sigmund O (2003) Topology optimization-theory: methods and applications. Springer, Berlin

Bico J, Marzolin C, Quéré D (1999) Pearl drops. Europhys Lett 47:220–226

Borrvall T, Petersson J (2003) Topology optimization of fluid in Stokes flow. Int J Numer Methods Fluids 41:77–107

Cadman J, Zhou S, Chen Y, Li Q (2013) On design of multi-functional microstructural materials. J Mater Sci 48:51–66

Cassie ABD, Baxter S (1944) Wettability of porous surfaces. Trans Faraday Soc 40:546

Cavalli A, Bøggilda P, Okkels F (2013) Topology optimization of robust superhydrophobic surfaces. Soft Matter 9:2234–2238

Chern SS, Chen WH, Lam KS (1999) Lectures on differential geometry. World Scientific Publishing

Christiansen AN, Bærentzen JA, Nobel-Jørgensen M, Aage N, Sigmund O (2015a) Combined shape and topology optimization of 3D structures. Comput Graph 46:25–35

Christiansen RE, Lazarov B, Jensen JS, Sigmund O (2015b) Creating geometrically robust designs for highly sensitive problems using topology optimization. Struct Multidiscip Optim 52:737–754

Clausen A, Andreassen E, Sigmund O (2017) Topology optimization of 3D shell structures with porous infill. Acta Mech Sin 33:778–791

Daoud F, Firl M, Bletzinger KU (2005) Filter techniques in shape optimization with CAD-free parametrization, 6Th World Congresses of Structural and Multidisciplinary Optimization. Rio de Janeiro, Brazil

Deng Y, Liu Z, Zhang P, Liu Y, Wu Y (2011) Topology optimization of unsteady incompressible Navier-Stokes flows. J Comput Phys 230:6688–6708

Deng Y, Liu Z, Liu Y, Wu Y (2014) Combination of topology optimization and optimal control method. J Comput Phys 257:374–399

Deng Y, Liu Z, Wu Y (2017) Topology optimization of capillary, two-phase flow problems. Commun Comput Phys 22:1413–1438

Deng Y, Liu Z, Wang Y, Duan H, Korvink JG (2019) Micro-textures inversely designed with overlayed-lithography manufacturability for wetting behavior in Cassie–Baxter status. Appl Math Model 74:621–640

Deng Y, Mager D, Bai Y, Zhou T, Liu Z, Wen L, Wu Y, Korvink JG (2018) Inversely designed micro-textures for robust Cassie-Baxter mode of super-hydrophobicity. Comput Methods Appl Mech Eng 341:113–132

Deng Y, Liu Z, Korvink JG (2020) Topology optimization on two-dimensional manifolds. Comput Methods Appl Mech Engrg 364:112937

Dienemann R, Schumacher A, Fiebig S (2017) Topology optimization for finding shell structures manufactured by deep drawing. Struct Multidisc Optim 56:473–485

Dilgen CB, Dilgen SB, Fuhrman DR, Sigmund O, Lazarov B (2018) Topology optimization of turbulent flows. Comput Methods Appl Mech Eng 331:363–393

Eral HB, 't Mannetje DJCM, Oh JM (2013) Contact angle hysteresis: a review of fundamentals and applications. Colloid Polym Sci 291:247–260

Feng X, Jiang L (2006) Design and creation of superwetting/antiwetting surfaces. Adv Mater 18:3063–3078

Gao T, Zhang W (2011) A mass constraint formulation for structural topology optimization with multiphase materials. Int J Numer Meth Eng 88:774–796

Gersborg-Hansen A, Bendsøe MP, Sigmund O (2006) Topology optimization of heat conduction problems using the finite volume method. Struct Multidisc Optim 31:251–259

Gibiansky LV, Sigmund O (2000) Multiphase composites with extremal bulk modulus. J Mech Phys Solids 48:461–498

Grünbaum B, Shephard GC (2016) Tilings and patterns, 2nd edn. Dover Publications, ISBN 9780486469812

Guest J, Prévost J, Belytschko T (2004) Achieving minimum length scale in topology optimization using nodal design variables and projection functions. Int J Numer Methods Eng 61:238–254

Guest J, Prévost J (2006) Topology optimization of creeping fluid flows using a Darcy-Stokes finite element. Int J Numer Methods Eng 66:461–484

Guo X, Zhao X, Zhang W, Yan J, Sun G (2015) Multi-scale robust design and optimization considering load uncertainties. Comput Methods Appl Mech Eng 283:994–1009

Hassani B, Tavakkoli SM, Ghasemnejad H (2013) Simultaneous shape and topology optimization of shell structures. Struct Multidisc Optim 48:221–233

Hebey E (1996) Sobolev spaces on Riemannian manifolds. Springer, Berlin

Hinze M, Pinnau R, Ulbrich M, Ulbrich S (2009) Optimization with PDE constraints. Springer, Berlin

Huang X, Zhou SW, Xie YM, Li Q (2013) Topology optimization of microstructures of cellular materials and composites for macrostructures. Comput Mater Sci 67:397–407

Hvejsel CF, Lund E (2011) Material interpolation schemes for unified topology and multi-material optimization. Struct Multidisc Optim 43:811–825

Jameson A, Vassberg A (2000) Studies of alternative numerical optimization methods applied to the Brachistochrone problem. Comput Fluid Dyn J 9:281–296

Kawata S, Sun HB, Tanaka T, Takada K (2001) Finer features for functional microdevices. Nature 412:697–698

Kreissl S, Pingen G, Maute K (2011) An explicit level-set approach for generalized shape optimization of fluids with the lattice Boltzmann method. Int J Numer Meth Fluids 65:496–519

Krog L, Olhoff N (1996) Optimum topology and reinforcement design of disk and plate structures with multiple stiffness and eigenfrequency objectives. Comput Struct 72:535–63

Laplace P (1806) Supplement to the tenth edition, Méchanique Céleste 10:1749–1827

Lazarov B, Sigmund O (2011) Filters in topology optimization based on Helmholtz type differential equations. Int J Numer Methods Eng 86:765–781

Lochner-Aldinger I, Schumacher A (2014) Homogenization method. In: Adriaenssens S, Block P, Veenendaal D, Williams C (eds) Shell structures for architecture-form finding and optimization. Routledge, New York

Lundgaard C, Alexandersen J, Zhou M, Andreasen CS, Sigmund O (2018) Revisiting density-based topology optimization for fluid-structure-interaction problems. Struct Multidisc Optim 58:969–995

Luo YJ, Kang Z, Yue ZF (2012) Maximal stiffness design of two-material structures by topology optimization with nonprobabilistic reliability. AIAA J. 50:1993–2003

Maute K, Ramm E (1997) Adaptive topology optimization of shell structures. AIAA J 35:1767–1773

Raulli M, Maute K (2005) Topology optimization of electrostatically actuated microsystems. Struct Multidisc Optim 30:342–359

Rodrigues H, Guedes JM, Bendsøe MP (2002) Hierarchical optimization of material and structure. Struct Multidisc Optim 24:1–10

Sigmund O (2007) Morphology-based black and white filters for topology optimization. Struct Multidiscip Optim 33:401–424

Sigmund O, Torquato S (1997) Design of materials with extreme thermal expansion using a three-phase topology optimization method. J Mech Phys Solids 45:1037–1067

Sigmund O, Maute K (2013) Topology optimization approaches — a comparative review. Struct Multidisc Optim 48:1031–1055

Sivapuram R, Dunning PD, Kim HA (2016) Simultaneous material and structural optimization by multiscale topology optimization. Struct Multidisc Optim 54:1267–1281

Svanberg K (1987) The method of moving asymptotes: a new method for structural optimization. Int J Numer Meth Eng 24:359–373

Toster J, Lewis D (2015) Investigation of roughness periodicity on the hydrophobic properties of surfaces. Aust J Chem 68:1228–1232

Vanhook SJ, Schatz MF, Swift JB, Mc Cormick WD, Swinney HL (1997) Long-wavelength surface-tension-driven Bé,nard convection: experiment and theory. J Fluid Mech 345:45–78

Vermaak N, Michailidis G, Parry G, Estevez R, Allaire G, Bréchet Y (2014) Material interface effects on the topology optimization of multi-phase structures using a level set method. Struct Multidisc Optim 50:623–644

Wang MY, Wang XM (2004) "Color" level sets: a multi-phase method for structural topology optimization with multiple materials. Comput Methods Appl Mech Eng 193:469–496

Wang F, Lazarov B, Sigmund O (2011) On projection methods, convergence and robust formulations in topology optimization. Struct Multidiscip Optim 43:767–784

Wang S, Liu K, Yao X, Jiang L (2015) Bioinspired surfaces with superwettability: new insight on theory, design, and applications. Chem Rev 115:8230–8293

Wenzel RN (1936) Resistance of solid surfaces to wetting by water. Ind Eng Chem 28:988

Wu D, Wu S, Chen QD, Zhao S, Zhang H, Jiao J, Piersol JA, Wang JN, Sun HB, Jiang L (2011) Facile creation of hierarchical PDMS microstructures with extreme underwater superoleophobicity for anti-oil application in microfluidic channels. Lab Chip 11:3873–3879

Wu Z, Xia L, Wang S, Shi T (2019) Topology optimization of hierarchical lattice structures with substructuring. Comput Methods Appl Mech Eng 345:602–617

Xia L, Breitkopf P (2015) Multiscale structural topology optimization with an approximate constitutive model for local material microstructure. Comput Methods Appl Mech Eng 286:147–167

Xu Z, Zhang W, Zhou Y, Zhu J (2019) Multiscale topology optimization using feature-driven method. Chinese Journal of Aeronautics. https://doi.org/10.1016/j.cja.2019.07.009

Yan X, Huang X, Zha Y, Xie YM (2014) Concurrent topology optimization of structures and their composite microstructures. Comput Struct 133:103–110

Yang K, Zhu J, Wu M, Zhang W (2018) Integrated optimization of actuators and structural topology of piezoelectric composite structures for static shape control. Comput Methods Appl Mech Eng 334:440–469

Yin L, Ananthasuresh GK (2011) Topology optimization of compliant mechanisms with multiple materials using a peak function material interpolation scheme. Struct Multidisc Optim 23:49–62

Yoon GH (2010) Topology optimization for stationary fluid–structure interaction problems using a new monolithic formulation. Int J Numer Meth Eng 82:591–616

Yoon GH (2016) Topology optimization for turbulent flow with Spalart-Allmaras model. Comput Methods Appl Mech Eng 303:288–311

Young T (1805) An essay on the cohesion of fluids. Phil Trans 95:65–87

Zhang W, Sun S (2006) Scale-related topology optimization of cellular materials and structures. Int J Numer Meth Eng 68:993–1011

Zhou SW, Wang MY (2007) Multimaterial structural topology optimization with a generalized Cahn-Hilliard model of multiphase transition. Struct Multidisc Optim 33:89–111

Zhu J, Zhang W, Beckers P, Chen Y, Guo Z (2008) Simultaneous design of components layout and supporting structures using coupled shape and topology optimization technique. Struct Multidisc Optim 36:29–41

Affiliations

Yongbo Deng[1,2] · Weihong Zhang[3] · Zhenyu Liu[2] · Jihong Zhu[3] · Jan G. Korvink[1]

[1] Institute of Microstructure Technology (IMT),
Karlsruhe Institute of Technology (KIT),
Hermann-von-Helmholtzplatz 1,
Eggenstein-Leopoldshafen, 76344, Germany

[2] State Key Laboratory of Applied Optics, Changchun Institute of
Optics, Fine Mechanics and Physics (CIOMP), Chinese Academy
of Sciences, 130033, Changchun, China

[3] State IJR Center of Aerospace Design and Additive Manufac-
turing, Northwestern Polytechnical University, Xi'an, Shaanxi,
710072 China